JGR Solid Earth

RESEARCH ARTICLE
10.1029/2022JB025664

Key Points:

- A high-resolution Lg attenuation model is developed beneath the Iranian Plateau
- Strong Lg attenuation characterizes tectonically active areas or recent magmatic zones
- Crustal thermal structure revealed by Lg attenuation links Cenozoic magmatism in Iran with sub-lithospheric mantle processes

Supporting Information:

Supporting Information may be found in the online version of this article.

Correspondence to:

L.-F. Zhao,
zhaolf@mail.iggcas.ac.cn

Citation:

Yang, G., Chen, L., Zhao, L.-F., Xie, X.-B., & Yao, Z.-X. (2023). Crustal Lg attenuation beneath the Iranian Plateau: Implications for Cenozoic magmatism related to slab subduction, slab break-off, and mantle flow. *Journal of Geophysical Research: Solid Earth*, *128*, e2022JB025664. https://doi.org/10.1029/2022JB025664

Received 21 SEP 2022
Accepted 14 MAR 2023

Author Contributions:

Conceptualization: Geng Yang, Ling Chen, Lian-Feng Zhao, Xiao-Bi Xie
Data curation: Geng Yang, Ling Chen, Lian-Feng Zhao
Formal analysis: Geng Yang
Funding acquisition: Ling Chen, Lian-Feng Zhao, Zhen-Xing Yao
Investigation: Geng Yang
Methodology: Geng Yang, Lian-Feng Zhao, Xiao-Bi Xie
Project Administration: Lian-Feng Zhao, Zhen-Xing Yao
Resources: Geng Yang
Software: Geng Yang, Lian-Feng Zhao
Supervision: Lian-Feng Zhao, Xiao-Bi Xie, Zhen-Xing Yao
Validation: Geng Yang
Visualization: Geng Yang
Writing – original draft: Geng Yang

Crustal Lg Attenuation Beneath the Iranian Plateau: Implications for Cenozoic Magmatism Related to Slab Subduction, Slab Break-Off, and Mantle Flow

Geng Yang[1,2], Ling Chen[2,3], Lian-Feng Zhao[1,4], Xiao-Bi Xie[5], and Zhen-Xing Yao[1]

[1]Key Laboratory of Earth and Planetary Physics, Institute of Geology and Geophysics, Chinese Academy of Sciences, Beijing, China, [2]College of Earth and Planetary Sciences, University of Chinese Academy of Sciences, Beijing, China, [3]State Key Laboratory of Lithosphere Evolution, Institute of Geology and Geophysics, Chinese Academy of Sciences, Beijing, China, [4]Heilongjiang Mohe Observatory of Geophysics, Institute of Geology and Geophysics, Chinese Academy of Sciences, Beijing, China, [5]Institute of Geophysics and Planetary Physics, University of California at Santa Cruz, Santa Cruz, CA, USA

Abstract Cenozoic magmatism is present across the Iranian Plateau but, despite playing an important role in the geodynamic evolution of the young plateau, remains poorly understood. In this study, the crustal thermal structure beneath the Iranian Plateau is investigated by high-resolution Lg-wave attenuation tomography using a newly compiled data set, which consists of records from three recent temporary seismic arrays (for a total of 197 stations) and previous regional networks. Strong Lg attenuation is mainly observed beneath the Zagros orogenic belt, Urumieh-Dokhtar magmatic arc (UDMA), Makran magmatic arc, Lut magmatic zone, and Alborz rearare magmatic belt, which covers not only tectonic boundary belts but also the active internal zones of the Iranian Plateau. Combining deep seismological observations and geochemical data, the strong crustal attenuation characteristics beneath the northwestern and southeastern UDMA suggest that Miocene–Quaternary magmatism was activated by slab detachment-induced upwelling after the cessation of oceanic subduction. Western Makran is characterized by strong Lg attenuation with a NE trend. The age of the Paleogene–Quaternary Makran volcanism decreases toward the NE and is likely related to the change in subduction dip. Diffuse magmatism and strong crustal attenuation are present in the northern Lut Block rather than the entire Lut–Afghan collision zone, which is likely associated with the accumulation of mantle magmas driven by the potential northward asthenospheric flow. In northern Iran, a strong attenuation anomaly spans the entire E–W Alborz magma belt, suggesting that partial crustal melting and mantle thermal sources may exist in this region.

Plain Language Summary The Iranian Plateau is located in the Middle East and is a part of the Alpine-Himalayan orogenic system. Intensive Cenozoic volcanic activity is characteristic of the Iranian Plateau, but the origination, storage, and transport of underground magma are poorly understood. Seismic attenuation is sensitive to high temperatures and partial melting and can be an indicator of the distribution of heat sources. In this study, we investigate the attenuation features of the crust with a new data set to constrain the crustal thermal structure beneath the Iranian Plateau by using a specific type of seismic wave (Lg) that travels within the crust. Hot crustal sources were observed beneath the Zagros orogenic belt and the four magmatic zones. Therefore, the origination of magmatism can be inferred based on the crustal attenuation distribution. Typically, the younger magmatism in the northwestern and southeastern Urumieh-Dokhtar magmatic arc was likely activated by deeper mantle upwelling, which may be related to plate kinematics at depth (slab detachment or break-off). On the southeastern edge of Iran, the Makran region is characterized by strong attenuation with a NE trend, where the volcanism also gets younger toward the NE. It is likely related to the dip change in oceanic plate subduction.

1. Introduction

Extensive magmatism typically occurs along continental margins and plate boundaries (Stern et al., 2021). Exploring the formation mechanism of magmatism can help us to understand plate processes at depth, such as slab subduction, dehydration, or detachment. However, around convergent plate boundaries, the distribution of heat sources in the lithosphere is less detectable than those in surface volcanic rocks and deep subduction structures (e.g., Chiu et al., 2013; Pang et al., 2013; Su et al., 2014).

Writing – review & editing: Ling Chen, Lian-Feng Zhao, Xiao-Bi Xie

As a part of the Alpine–Himalayan orogenic system (Figure 1a), the Iranian Plateau has experienced distinctive geodynamic evolution, including crust formation, terrane accretion, subduction initiation, and continental collision. During approximately 35–20 Ma, the collision between the Arabian plate and central Iran marked the final demise of the ancient Neotethys Ocean (Stern et al., 2021). The subduction of the Neotethys Ocean and the later continental collision triggered widespread Cenozoic volcanism across the Iranian Plateau. The associated structure at depth and the mechanism of Cenozoic magmatism are essential to resolve the geodynamic evolution of the young plateau.

Cenozoic igneous rocks crop out mainly in the Urumieh-Dokhtar magmatic arc (UDMA), Alborz magmatic belt, Makran magmatic arc, and Lut magmatic zone (Figure 1b). The longest NW-SE UDMA (~55-5 Ma) extends ~1,500 km across central Iran, terminating at the Makran subduction region in the southeast and the Talesh-Alborz Mountains in the northwest (Asadi et al., 2014; Chiu et al., 2013; Monsef et al., 2018; Pang et al., 2013). Beneath the Zagros fold-thrust belt (ZFTB), two high-velocity anomalies extending up to 600 km reveal that the shallower Arabian plate has subducted to approximately 200 km and that the Neotethys oceanic slab remains in the deep mantle at approximately 300–600 km (e.g., Alinaghi et al., 2007; Mahmoodabadi et al., 2019). The early Cenozoic volcanoes around the UDMA are fed by mantle wedge melting induced by Neotethys subduction (e.g., Asadi et al., 2014), and the late Cenozoic UDMA was possibly triggered by asthenospheric upwelling associated with slab rollback (e.g., S. Babazadeh et al., 2017), changes in subduction angle (Shahabpour, 2007), slab break-off (Omrani et al., 2008), and crustal thickening (e.g., Chiu et al., 2013). It is difficult to choose among these models without understanding the detailed thermal structure. The slightly arcuate Makran accretionary region in southeastern Iran is underplated by the active northward subduction of the Oman Sea (Burg, 2018; McCall, 1997), which began during the Cretaceous and continues today (e.g., Alavi, 2007; Ricou, 1994). The formation of the Makran magmatic belt and the surrounding Bazman, Taftan, and Koh-e-Nadir volcanoes (Figure 1b) resulted from low-angle or flat-slab subduction of the Arabian plate (Oman Sea) (Abedi & Bahroudi, 2016; Regard et al., 2010; Yamini-Fard et al., 2007). Across the W–E Makran subduction zone, the slab descends into the mantle at different distances and dipping angles from the trench and further affects the distribution of surface volcanism (e.g., Motaghi et al., 2020; Mousavi et al., 2022). However, the magmatic accumulation pattern in the crust and mantle is not well documented. In eastern Iran, the N–S-trending Lut Block might have overridden the subducted Early Cretaceous Sistan Ocean and then collided with the Afghan Block after the ocean closed (S. A. Babazadeh & Wever, 2004; Moghaddam et al., 2021). The formation mechanism behind Lut volcanism is also controversial. The Cenozoic magmatism in the Lut Block was possibly triggered by the westward subduction of the ancient Sistan oceanic lithosphere (e.g., Samiee et al., 2016) or lithospheric delamination caused by the Lut–Afghan collision (Pang et al., 2013). Furthermore, in contrast with linear magmatic belts, the diffuse distribution of the Lut volcanic rocks may also indicate a special magma migration pattern. In northern Iran, the E–W Alborz rearc magmatic belt behind the UDMA developed in response to Paleogene back-arc extension and crustal thinning (e.g., Asiabanha & Foden, 2012). The source region of Alborz magmas may be influenced by various components, including a deeply subducted lithosphere and partial melts of the lithosphere in an extensional back-arc setting (Asiabanha & Foden, 2012). This poorly understood magmatism in the Iranian Plateau spatially connects deep structures and surface volcanoes and spans multiple geological epochs, contributing to our understanding of the formation of the young plateau.

Determining the current crustal thermal structure within the plateau is an effective way to retrospectively examine younger magma activity (Su et al., 2014) and is an important way to link the deep large-scale mantle structure and surface volcanic activity. A large number of geophysical studies have been conducted in and around the Iranian Plateau, including seismic velocity tomography (e.g., Al-Lazki et al., 2014; Alinaghi et al., 2007; Amini et al., 2012; Mahmoodabadi et al., 2019; Pei et al., 2011), seismic anisotropy investigation (e.g., Gao et al., 2022; Kaviani et al., 2021), attenuation tomography (e.g., Kaviani et al., 2015; Pasyanos et al., 2009, 2021; Sandvol et al., 2001; Zhao & Xie, 2016), receiver function imaging (e.g., Taghizadeh-Farahmand et al., 2015; Wu et al., 2021), gravity inversion (e.g., Jiménez-Munt et al., 2012), and GPS data analysis (e.g., Vernant et al., 2004). Compared with seismic velocity related to the elastic properties of the Earth, seismic attenuation has special advantages in detecting lithospheric thermodynamics, including outstanding sensitivities to temperature, partial melting, and fluid and magma movements (e.g., Boyd et al., 2004). Therefore, investigating the characteristics of attenuations could provide important constraints on thermal-related regional tectonics and dynamic evolution.

Regional Lg-waves are ideal for characterizing attenuation in the crust (Furumura & Kennett, 1997) because they have the most prominent seismic energy in high-frequency seismograms and are usually understood as the sum of supercritical reflected S-waves trapped within the crustal waveguide (Bouchon, 1982) or the surface wave overtones traveling within the continental crust (e.g., Knopoff et al., 1973). Amplitude variations in Lg-waves and

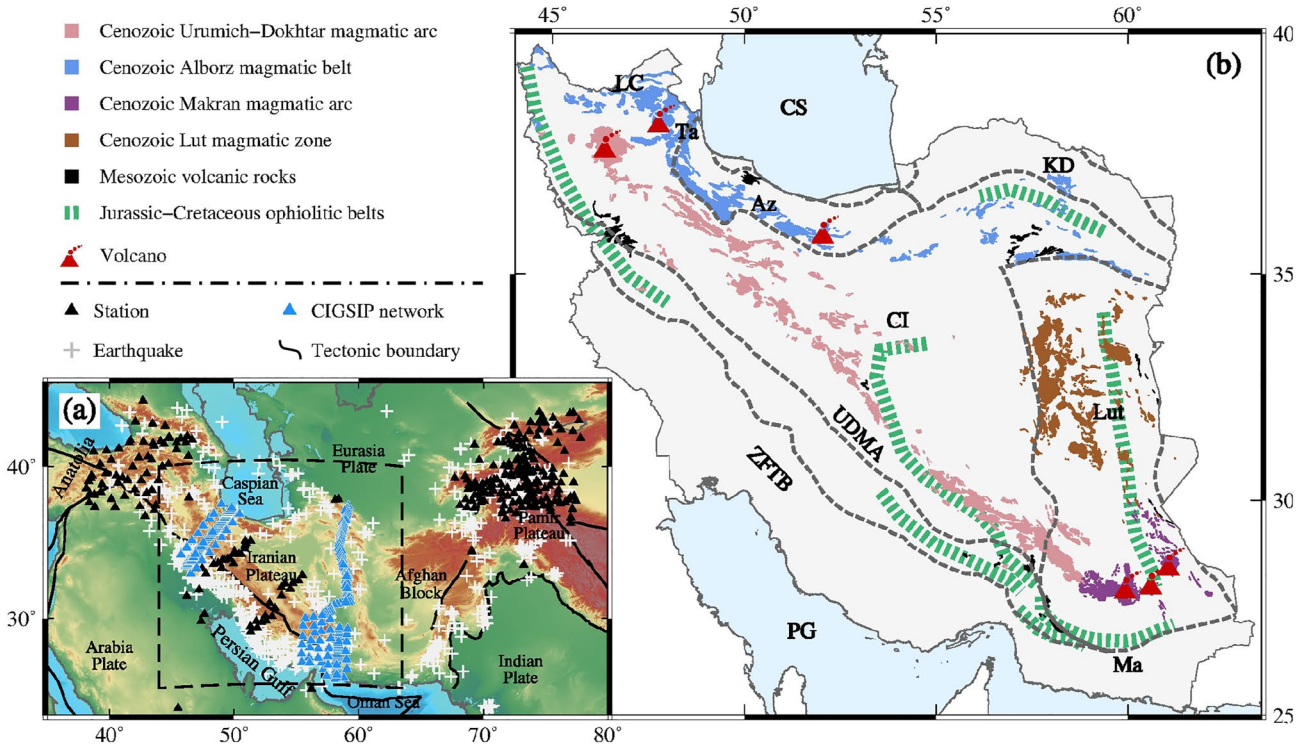

Figure 1. (a) Topographic map showing the study area and the locations of seismic stations and earthquakes. (b) Main magmatic belts and ophiolite belts in the Iranian Plateau. CS, Caspian Sea; PG, Persian Gulf; OS, Oman Sea; LC, Lesser Caucasus Mountains; Ta, Talesh Mountains; Az, Alborz Mountains; KD, Kopet-Dogh Mountains; CI, Central Iranian Basin; Lut, Lut Block; UDMA, Urumieh-Dokhtar magmatic arc; ZFTB, Zagros fold-thrust belt; Ma, Makran region.

Lg-coda have been widely used to measure the attenuation and scattering structure of the crust (e.g., Al-Damegh et al., 2004; Kaviani et al., 2015; Pasyanos et al., 2009; Sandvol et al., 2001; Zhao & Xie, 2016). In general, a higher quality factor (Q) of Lg-waves corresponds to weaker attenuation, representing a stable and colder crustal structure, while a lower Q value corresponds to stronger attenuation, indicating unstable and high-temperature tectonic environments. The Iranian Plateau typically represents a strong attenuation (low Q) area, which corresponds to an active orogenic system (e.g., Kaviani et al., 2015; Pasyanos et al., 2021; Sandvol et al., 2001; Zhao & Xie, 2016). Lg/Pg attenuation tomography has revealed an entire weak Lg region with Lg/Pg ratios of 1.5–2.0 in the Iranian Plateau (Al-Damegh et al., 2004; Sandvol et al., 2001). Similarly, most of Iran shows low Q_{Lg} (<300) in the 1.0 Hz Lg attenuation models (Kaviani et al., 2015; Pasyanos et al., 2009). The resolution of the previous broadband Lg attenuation image is only 6° × 6° on the Iranian Plateau (Zhao & Xie, 2016). P- and S-wave attenuation models of the crust and upper mantle also reveal only large-scale attenuation features (e.g., Pasyanos et al., 2021). The resolutions of attenuation tomography have been limited primarily by the sparse station distribution in Iran (e.g., Zhao & Xie, 2016), which is insufficient for exploring the detailed thermal distributions associated with magmatism.

In this study, we collected a large amount of new broadband waveform data from three seismic arrays in Iran that have been used in studies of receiver functions and seismic anisotropy (Gao et al., 2022; Sadeghi-Bagherabadi et al., 2018; Wu et al., 2021). Benefitting from these seismic networks (Figure 1a), it is an unprecedented opportunity to image the high-resolution crustal Lg-wave attenuation structure beneath the Iranian Plateau. Combined with previous geochemical analysis of surface volcanic rocks and deep geophysical observations, the crustal attenuation features complement constraints on crustal thermal structure and improve our understanding of the evolution of Cenozoic magmatism within the Iranian Plateau.

2. Data and Method

2.1. Regional Waveform Data

We investigated the quality factor Q of regional Lg-waves by allocating the spectral amplitude to multiple factors related to amplitude attenuation. Some previous attenuation studies were limited by the few stations in Iran,

which made it difficult to improve imaging resolution (e.g., Zhao & Xie, 2016). In this study, we collected 38,928 vertical-component waveforms from 859 seismic events ($4.3 \leq m_b \leq 6.5$) that occurred in and around the Iranian Plateau between October 2014 and September 2020 (Figure 1a and Table S1 in Supporting Information S2). The events were selected from the Harvard Centroid Moment Tensor Catalog (CMT) (Ekstrom et al., 2012) with depths shallower than the Moho discontinuity (Laske et al., 2013). The range of earthquake selection was from 35° to 80° east longitude and from 23° to 45° north latitude, and the epicentral distances were between 200 and 2,000 km. The 305 stations were provided by the Incorporated Research Institutions for Seismology (IRIS) data management center, the German Research Centre for Geoscience, the International Seismological Centre, and the International Federation of Digital Seismograph Networks. However, some permanent station data from the Iranian Seismological Center could not be collected in this study but were used in previous studies (e.g., Kaviani et al., 2015). We used a new data set from some mobile stations in Iran to increase the tomographic resolution. Under the China-Iran Geological and Geophysical Survey in the Iranian Plateau (CIGSIP) project, the Institute of Geophysics and Geology of the Chinese Academy of Sciences, the Geological Survey of Iran, and the Institute for Advanced Studies in Basic Sciences established three seismic networks during 2013–2018, including 65 and 132 broadband stations in western and eastern Iran, respectively (Figure 1a). The western NE–SW array was operated continuously between September 2013 and October 2014, covering a narrow belt over the Zagros collision zone and the region of the Alborz Mountains. The eastern two arrays (operating from July 2015 to September 2016 and from March 2017 to October 2018, respectively) trends roughly N–S from the Kopeh Dagh in the north to the Makran accretionary wedge in the south, and passes through the Lut Block. The average station spacing is approximately 15 km for the northeastern array and the southeastern main sub-array, and increases to ~50–80 km for the southeastern offline sub-arrays. All the stations were equipped with Trillium 120PA seismometers (120 s–175 Hz) and Taurus digital seismographs. Data on these stations (hereafter called CIGSIP stations) have been successfully used in studies of receiver functions and seismic anisotropy in this region (Gao et al., 2022; Sadeghi-Bagherabadi et al., 2018; Wu et al., 2021). Detailed station information is listed in Table S2 in Supporting Information S2. Example waveforms for two selected events show that both the global networks and the CIGSIP network recorded clear Lg waveform signals (Figure S1 in Supporting Information S1), which have maximum energy within the regional distances. New waveform data collected at densely spaced stations can greatly improve the constraints on lateral variations in crustal attenuation characteristics.

2.2. Lg-Wave Spectral Amplitude

The measurement of the Lg amplitude follows the method of Zhao, Xie, He, et al. (2013). Within the regional distance of 200–2,000 km, Lg energy is usually prominent in the group velocity window of 3.6–3.0 km/s. Considering the uncertainties in the origin time, epicenter location, source depth, tectonic complexity of the study area, etc., a floating group velocity window was used (Zhao & Xie, 2016). We first removed instrument responses between 0.01 and 100.0 Hz before the amplitude measurements. The vertical-component velocity waveforms were bandpass filtered between 0.5 and 5.0 Hz to determine the Lg-wave window (Figure 2a). We used a 0.6 km/s-long group velocity window to scan the waveform between 3.7 and 2.8 km/s (from 3.7–3.1 km/s to 3.4–2.8 km/s), with a step of 0.01 km/s. The sum of squares of amplitudes $\sum A_i^2$ in individual windows was calculated to determine the Lg-wave window based on the maximum energy (Figure 2a). Some Lg-wave windows may contain a small part of Lg-coda, but the Lg-wave energies are dominant. The noise signals are extracted from the pre-P arrival window with the same length (Figures 2b and 2c). The displacement fast Fourier transform spectra of both the Lg and noise are calculated (Figure 2d). Note that no additional filter is used in the amplitude measurements. To facilitate subsequent processing, 58 discrete amplitude data were sampled at equal intervals in the logarithmic frequency domain between 0.05 and 10.0 Hz as well as the noise series. Assuming that the noise is random and stationary over a certain time period, noise correction can be performed using the difference between the amplitude energy and the noise energy: $A_s^2(f) = A_o^2(f) - A_n^2(f)$, where the subscripts s, o, and n denote the clear, observed and noisy signals, respectively (Ringdal et al., 1992). A signal-to-noise ratio (SNR) of 2.0 is used as a criterion for Lg data selection (Figure 2e), and the amplitudes of the clear Lg signal are then obtained after removing the noise (Figure 2f). These processes significantly reduced the amount of available data at higher frequencies due to the strong attenuation of high-frequency signals (Figure S2 in Supporting Information S1). The elimination of bad data is an effective way to ensure data quality when building an amplitude data set. A manifestation of poor amplitude measurements is a considerable difference from other amplitudes with similar epicentral distances. Therefore, we fit the linear regression equation for amplitude and epicentral distance

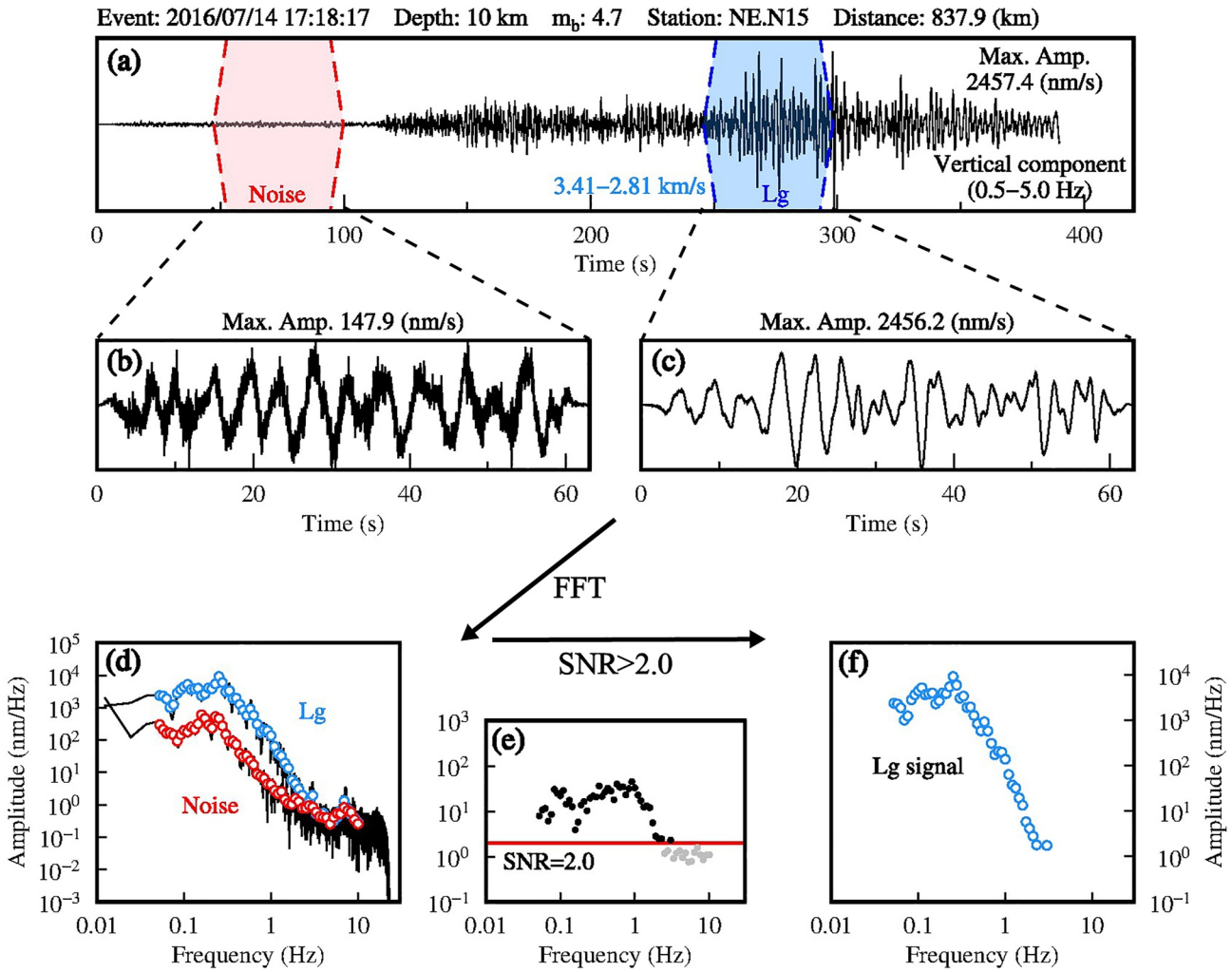

Figure 2. Lg-wave spectral amplitude measurement. (a) Vertical-component velocity seismogram of the event on 14 07 2016 recorded at station NE. N15 in the eastern CIGSIP network. The focal depth is 10 km, and the body-wave magnitude is 4.7. The red and blue windows sample the noise and Lg signal, respectively. (b)–(c) Noise and Lg signals sampled by two 0.6 km/s group velocity windows. (d) Lg and noise spectra. (e) Signal-to-noise ratio (SNR). Data with an SNR < 2.0 (gray dots) are discarded. (f) Lg spectra after noise correction.

in the logarithmic domain and remove the poor data that deviate more than three times the standard deviation from the fitted average.

The spectral amplitude of the Lg-wave can be expressed as (Xie, 1993):

$$A(f) = S(f) \cdot G(\Delta, f) \cdot \Gamma(\Delta, f) \cdot P(f) \cdot r(f), \quad (1)$$

where $A(f)$ is the amplitude at frequency f, $S(f)$ is the source spectrum, $G(\Delta, f)$ is the geometric spreading factor relative to epicentral distance Δ and frequency f, $\Gamma(\Delta, f)$ is the attenuation term, $P(f)$ is the site response and $r(f)$ is the random effect. The source term S(f) can be further expressed as: $S(f) = M_0/4\pi\rho\beta^3 \cdot \left[1 + \frac{f^2}{f_c^2}\right]^{-1}$ (Sereno et al., 1988), where M_0 represents the seismic moment; ρ is the density, taking 2.7g/cm^3 for the crust (Sereno et al., 1988); β is the average crustal shear wave velocity; and f_c is the corner frequency. The geometrical spreading is $G = (\Delta_0\Delta)^{-1/2}$, with Δ representing the epicentral distance and Δ_0 representing the reference distance fixed at 100 km (Pasyanos et al., 2009; Street et al., 1975; Xie, 1993; Zhao, Xie, Wang, et al., 2013). The attenuation term $\Gamma(\Delta, f)$ can be expressed as: $\Gamma(\Delta, f) = \exp\left[-\frac{\pi f}{\beta} B(\Delta, f)\right]$, where $B(\Delta,f)$ is the integral of attenuation over the great circle path: $B(\Delta, f) = \int_{\text{ray}} \frac{ds}{Q(f)}$. The frequency-dependent quality factor $Q(f)$ can be written in a power form: $Q(f) = Q_0 f^{\eta}$, where Q_0 and η are the Q value at 1 Hz and the frequency-dependent coefficient

(Zhao, Xie, He, et al., 2013), respectively. Two stations i and j recorded the same event at different epicentral distances and similar azimuth directions (<15°). When the two stations are not aligned perfectly with the event, as shown in Supporting Information S1 (Figure S3), we set a reference point l on the ray path kj, with its distance kl equal to the distance ki. Then, we set a tolerance by requiring the distance between points i and l to be within a half-grid space (Xie et al., 2004; Zhao, Xie, Wang, et al., 2013). The two-station spectral ratio can be expressed by:

$$\frac{A_i}{A_j} = \left(\frac{\Delta_i}{\Delta_j}\right)^{-\frac{1}{2}} \Gamma_{ij} \left(\frac{P_i}{P_j}\right) = \left(\frac{\Delta_i}{\Delta_j}\right)^{-\frac{1}{2}} \cdot \exp\left[\frac{-\pi f}{\beta} \int_j^i \frac{ds}{Q(\mathrm{x}, \mathrm{y}, f)}\right], \tag{2}$$

where Γ_{ij} represents the contribution from the attenuation between stations i and j (Zhao, Xie, He, et al., 2013).

2.3. Q_{Lg} Inversion

The single-station amplitudes can provide dense ray path coverage, and the two-station amplitude ratios can reduce the tradeoff between source and attenuation, together improving the resolution and confidence of attenuation imaging. We linearize Equations 1 and 2 in the logarithmic domain to establish the single- and two-station inversion systems. For the single-station data set, applying the natural logarithm to Equation 1, we have:

$$\ln[A(f)] - \ln[G(\Delta, f)] = \ln[S(f)] - \frac{\pi f}{\beta} B(\Delta, f). \tag{3}$$

The attenuation and source function can be further separated into a background part and a perturbation:

$$\frac{1}{Q(x, y, f)} \approx \frac{1}{Q^0(x, y, f)} - \frac{\delta Q(x, y, f)}{[Q^0(x, y, f)]^2}, \tag{4}$$

and:

$$\ln[S(f)] = \ln\left[S^0(f)\right] + \delta \ln[S(f)]. \tag{5}$$

Therefore, Equation 3 can be further expressed as:

$$\ln[A(f)] - \ln[G(\Delta, f)] - \ln\left[S^0(f)\right] + \frac{\pi f}{\beta} B^0(\Delta, f) = \delta \ln[S(f)] - \frac{\pi f}{\beta} \delta B(\Delta, f), \tag{6}$$

where variables with superscript 0 denote their values in the initial model or the transition model from a previous iteration, δQ is the perturbation of Q_{Lg}, $\delta \ln[S(f)]$ is the perturbation of the logarithmic Lg source function, and:

$$\delta B(\Delta, f) = \sum_{n=1}^{N} \int_n \frac{\delta Q(x, y, f)}{[Q^0(x, y, f)]^2} ds. \tag{7}$$

The integral in Equation 7 was calculated using the bilinear function in each rectangle:

$$Q(x, y) = \sum_{p=1}^{4} a_p w_p(x, y), \tag{8}$$

where $w_1 = 1$, $w_2 = x$, $w_3 = y$, $w_4 = xy$, and a_p are the interpolation parameters obtained from Q_{Lg} values. For multiple sources and stations, we can combine both Equations 6 and 7 into a linear system:

$$\boldsymbol{H}_s = \boldsymbol{A}_s \cdot \delta \boldsymbol{Q} + \boldsymbol{E} \cdot \delta \boldsymbol{S}, \tag{9}$$

where $\boldsymbol{H}_s$ is a vector composed of residuals between the observed and synthesized Lg spectra. Its elements are:

$$h_j = \ln\left[A_j(f)\right] - \ln\left[G_j(\Delta, f)\right] - \ln\left[S_k^0(f)\right] + \frac{\pi f}{\beta} B_j^0(\Delta, f), \tag{10}$$

where j and k are the indices for the rays and sources, respectively. The matrices $\boldsymbol{A}_s$ and $\boldsymbol{E}$ set up the relationships between $\delta\boldsymbol{Q}$ and $\boldsymbol{H}_s$ and between $\delta\boldsymbol{S}$ and $\boldsymbol{H}_s$, respectively. Similarly, we can create a linear system for the two-station data set:

$$\boldsymbol{H}_t = \boldsymbol{A}_t \cdot \delta\boldsymbol{Q}, \tag{11}$$

where $\boldsymbol{H}_t$ is a vector composed of residuals between observed and synthetic spectral ratios, and the matrix $\boldsymbol{A}_t$ can be obtained by discretizing Equation 2. Combining Equations 9 and 11, we obtain a hybrid tomography equation:

$$\begin{bmatrix} \boldsymbol{H}_s \\ \boldsymbol{H}_t \end{bmatrix} = \begin{bmatrix} \boldsymbol{A}_s \\ \boldsymbol{A}_t \end{bmatrix} \cdot \delta\boldsymbol{Q} + \begin{bmatrix} \boldsymbol{E} \\ 0 \end{bmatrix} \cdot \delta\boldsymbol{S}. \tag{12}$$

To solve the inverse problem, we started from a unit source function and an initial constant Q_{Lg} model obtained based on linear regression of the interstation amplitude ratio data (e.g., Zhao, Xie, Wang, et al., 2013). The residual vector between the observed and synthetic spectral amplitudes, $\boldsymbol{b} = \begin{bmatrix} \boldsymbol{H}_s \\ \boldsymbol{H}_t \end{bmatrix}$, can be obtained to solve the model modification vector, $\boldsymbol{m} = \begin{bmatrix} \delta\boldsymbol{Q} \\ \delta\boldsymbol{S} \end{bmatrix}$. A coefficient matrix, $\boldsymbol{A} = \begin{bmatrix} \boldsymbol{A}_s & \boldsymbol{E} \\ \boldsymbol{A}_t & 0 \end{bmatrix}$, can be used to simplify Equation 12 as:

$$\boldsymbol{A}\boldsymbol{m} = \boldsymbol{b}. \tag{13}$$

Single- and two-station data are jointly solved by the least squares orthogonal factorization inversion method (Paige & Saunders, 1982) at each frequency independently. The grid size was set to 1.0° × 1.0°. During the inversion, a damping parameter λ was used for regularization by minimizing:

$$\left\| \begin{bmatrix} \boldsymbol{A} \\ \lambda\boldsymbol{I} \end{bmatrix} \boldsymbol{m} - \begin{bmatrix} \boldsymbol{b} \\ 0 \end{bmatrix} \right\|_2, \tag{14}$$

where $\boldsymbol{I}$ is an identity matrix. We determined the damping parameter λ by considering the tradeoff between variance reduction and model norm. Based on the simplified inversion matrix equation $\boldsymbol{A}\boldsymbol{m} = \boldsymbol{b}$, the L-curve was obtained using the residual norm $\|\boldsymbol{A}\boldsymbol{m} - \boldsymbol{b}\|_2$ versus the model norm $\|\boldsymbol{m}\|_2$ with different damping parameters. For example, we chose the turning point of the L-curve as the optimal initial damping parameter at 1.0 Hz (Figure S4 in Supporting Information S1). Smaller damping values were used in subsequent iterations to ensure a better data fit while preserving robust anomaly features. As the number of iterations increases, the damping value decreases gradually. During each iteration, we also applied the first-order linear smoothness constraints to the solution along the longitudinal and latitudinal directions (e.g., Zhao et al., 2010).

The resulting source functions are shown in Supporting Information S1 (Figure S5), and the seismic moment and corner frequency for each event were further inverted (Figure S6 in Supporting Information S1 and Table S1 in Supporting Information S2). Note that the sum of all logarithmic site responses $\sum_{i=1}^{N} \ln P_i$ can be assumed to be zero (Ottemöller et al., 2002; Zhang et al., 2022; Zhao & Mousavi, 2018). Therefore, we assumed the sum of the perturbation of site responses (in logarithmic form) $\sum_{i=1}^{N} \delta \ln P_i = 0$ and simultaneously controlled the relative variation in site responses during the inversion, $\sum_{i=1}^{N} \delta|\ln P_i| < \varepsilon$, where ε is an empirical value for normalizing the site responses. We then pushed the unsolved residuals into the site term after the tomographic inversion. That is, the site response for each station was finally determined based on both the obtained source and attenuation terms (Figure S7 in Supporting Information S1 and Table S2 in Supporting Information S2).

After the inversion, the amplitude residuals are closer to the Gaussian distribution, and the root mean square (rms) values of the total residuals at all 58 frequencies are significantly reduced (Figure 3). The rms residuals decrease from 1.73, 1.37, and 1.44 to 0.52, 0.57, and 0.62 at 0.5, 1.0, and 1.5 Hz, respectively. We conducted checkerboard tests to analyze the resolution and reliability of the inversion system by adding 7% positive/negative

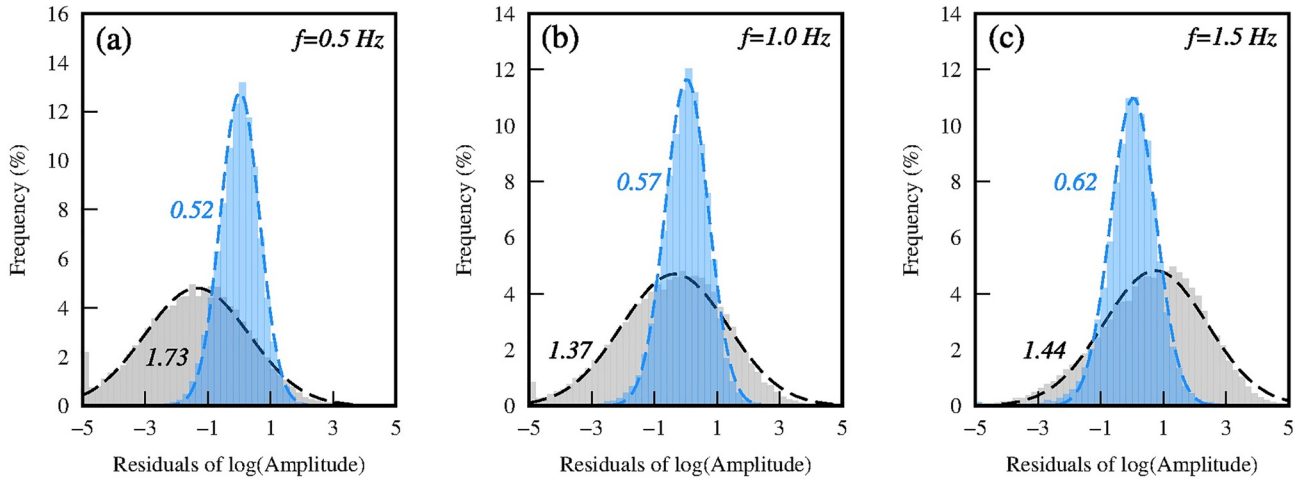

Figure 3. Histograms of the Lg spectral amplitude misfits before (gray) and after (blue) inversions at 0.5, 1.0, and 1.5 Hz, respectively. Dashed lines represent the best-fitting normal curves and adjacent labels denote the root mean square residuals.

perturbations to a constant background Q model (e.g., He et al., 2021; Zhao, Xie, He, et al., 2013). With the same sources, stations and ray paths as in the real data set, the synthetized Lg spectral amplitudes can partially recover the 1.0° × 1.0° checkerboard model in the area covered by relatively dense ray paths and can fully recover the 2.0° × 2.0° checkerboard model across the entire Iranian Plateau (Figure 4).

3. Results

3.1. Q_{Lg} Images at Individual Frequencies

A broadband Q_{Lg} model is constructed for the crust in and around the Iranian Plateau at 58 frequencies between 0.05 and 10.0 Hz. Lg-wave attenuation has strong frequency dependence. As shown in Figure 5, we grouped Q_{Lg} values and calculated average Q_{Lg} for six selected tectonic units, including the Eurasian Plate, Arabian Plate, Iranian Plateau, Afghan Block, Pamir Plateau, and Anatolian Plateau (Hatzfeld & Molnar, 2010). Although the power law relation $Q(f) = Q_0 f^{\eta}$ seems to be overly simple for predicting the Q_{Lg}-frequency trend between 0.05 and 10.0 Hz, it can be adopted within a relatively narrow frequency band, such as between 0.2 and 2.0 Hz (e.g., Pasyanos et al., 2009; Zhao et al., 2010). For individual tectonic units in Iran, the resulting η within 0.2–2.0 Hz ranges from 0.23 to 0.87 (Table S3 in Supporting Information S1). The average Q_0 (Q_{Lg} at 1.0 Hz) values of the stable Eurasian and Arabian plates are 562 and 457, respectively. They are much higher than those of the active Afghan Block (254) and Pamir (193) and Anatolian (115) Plateaus. The Iranian Plateau also has a lower Q_0 value (322), and relatively larger standard deviations indicate dramatic variations in the crustal attenuation signature, which can help us to understand the complicated crustal thermal structure in the Iranian Plateau. In the Afghan Block and Anatolian and Iranian Plateaus, the low Q_0 also corresponds well to the low velocities of Pn waves (Table S3 in Supporting Information S1, Pei et al., 2011).

In this study, the range from 0.2 to 2.0 Hz was selected as the dominant frequency band for our broadband Lg-wave attenuation model (e.g., Zhao & Xie, 2016; Zhao, Xie, He, et al., 2013). First, Lg attenuation between 0.2 and 2.0 Hz can sufficiently characterize the individual tectonic units (Figure 5h). At frequencies higher than 2.0 Hz, the Q_{Lg} curves are close to each other, whereas at low frequencies, the Lg-wave amplitude is strongly influenced by surface wave energy (e.g., Rayleigh wave), especially for basin areas with thick sedimentary layers (Cao & Muirhead, 1993; Shapiro et al., 1996; Zhao & Xie, 2016; Zhao et al., 2010). For example, the Caspian Sea, which has a thicker sedimentary layer, is characterized by strong attenuation at 0.1 Hz (Figure S8 in Supporting Information S1). Due to the strong attenuation of high-frequency signals, the SNR of the amplitudes decreases with increasing frequency (Figure 2e). The amount of available data at higher frequencies (>2.0 Hz) was significantly reduced (Figure S3 in Supporting Information S1). The raypath coverage is very sparse at higher frequencies, and the imaging has relatively lower resolution (Figure S8 in Supporting Information S1). In summary, the crustal attenuation model has relatively low resolution at lower and higher frequencies. Such a low-resolution Lg attenuation model

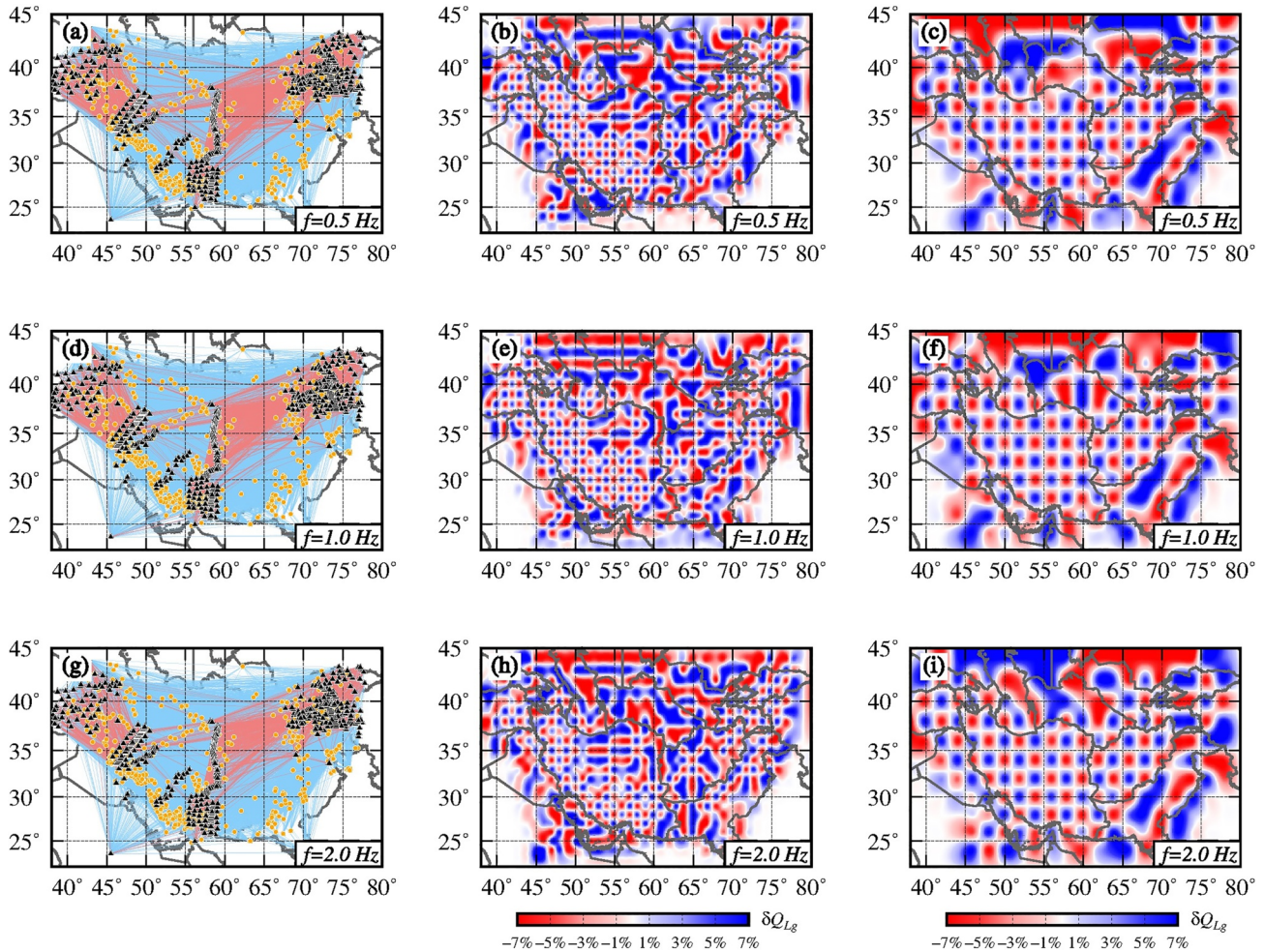

Figure 4. Ray-path coverages (left column) and checkerboard resolution analyses at 0.5, 1.0, and 1.5 Hz. The blue and red lines represent the single-station and dual-station paths, respectively. The orange dots and black triangles represent earthquakes and stations, respectively. The 1.0° × 1.0° (middle column) and 2.0° × 2.0° (right column) checkerboards of the Q perturbations are exhibited.

can be used to investigate the high-frequency fall-off rate of the source spectra but is not suitable for constraining the crustal thermal structure. Previous studies also tend to choose a frequency band of approximately 1.0 Hz as the dominant band for Lg-wave attenuation (e.g., Kaviani et al., 2015; Xie et al., 2004; Zhao & Xie, 2016).

Figure 6 illustrates four selected Q_{Lg} maps at 0.5, 1.0, 1.5, and 2.0 Hz, respectively. The Eurasian plate in the north shows prominent weak attenuation characteristics, in which the maximum Q_{Lg} can reach approximately twice the regional average. By comparison, the Anatolian Plateau, Iranian Plateau, Afghan Block, and Pamir Plateau all exhibit relatively lower Q_{Lg} than the surrounding stable Arabian and Eurasian Plates, which is consistent with previous studies (Kaviani et al., 2015; Pasyanos et al., 2021; Zhao & Xie, 2016). The lateral variations in crustal attenuation at each frequency are generally similar, but some specific zones vary with frequency. The south Caspian Sea shows strong attenuation features and changes to weak attenuation at higher frequencies. Similarly, the central Afghan Block changes from lower Q_{Lg} to higher Q_{Lg} as the frequency increases. Overall, the Iranian Plateau shows strong attenuation, but parts of central Iran are revealed as stable structures with high Q_{Lg}, which are more pronounced at higher frequencies. The low Q_{Lg} range beneath the ZFTB decreases with increasing frequency. The imaging resolutions were limited at higher frequencies, and some small-scale anomalies could not be revealed. Therefore, the lateral variation of attenuation seems "smoother" or otherwise lacks detail.

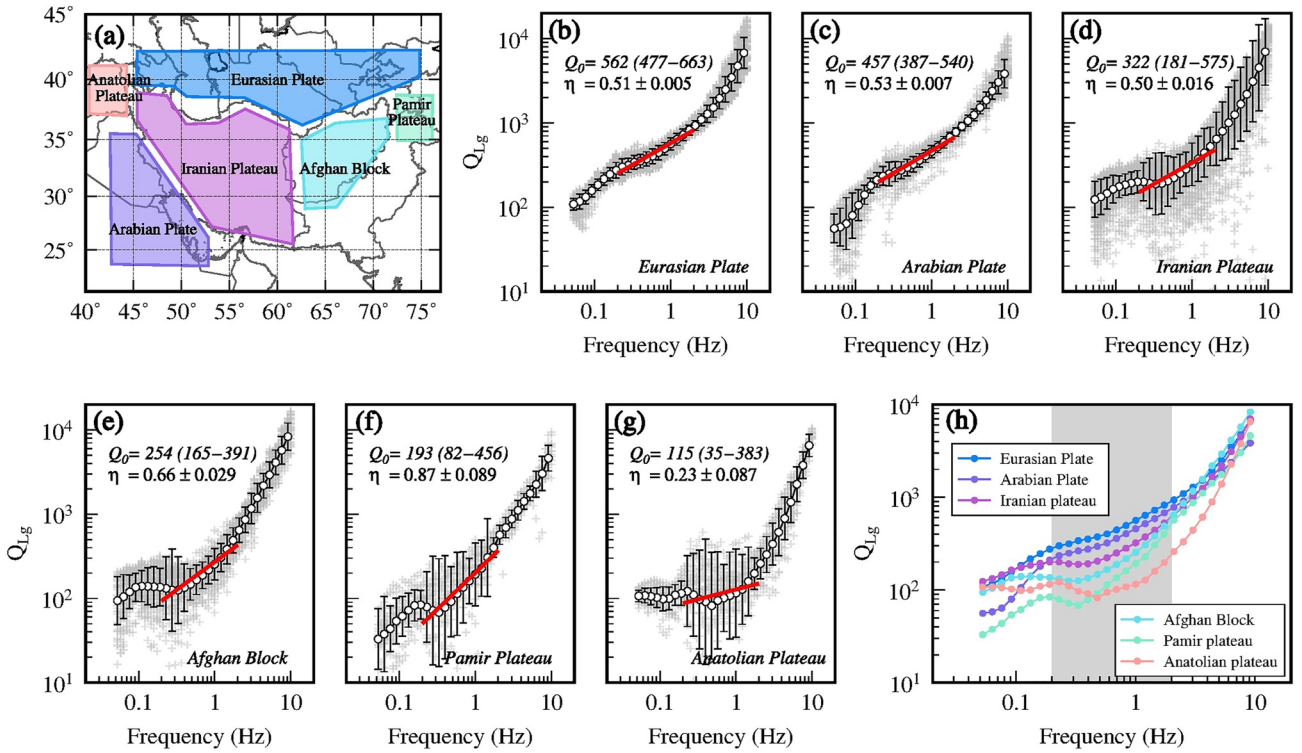

Figure 5. Frequency-dependent Q_{Lg} for selected tectonic units. (a) Map showing the locations of the geological units for Q_{Lg} statistics. (b)–(g) The directly inverted Q_{Lg} values (gray crosses) are plotted for individual tectonic units along with mean values within narrow frequency bands (white circles) and their logarithmic standard deviations (error bars). The power-law models $Q(f) = Q_0 f^{\eta}$ between 0.2 and 2.0 Hz (red line) are also plotted. Both Q_0 and the frequency-dependent parameter η are labeled on each panel. (h) Comparison of the mean Q_{Lg} values of the six tectonic units. The highlight frequency range of 0.2–2.0 Hz was selected as the dominant band for the Lg-wave attenuation model.

3.2. Broadband Q_{Lg} Distribution

The broadband Q_{Lg} model was obtained by calculating the logarithmic average of the Q_{Lg} values between 0.2 and 2.0 Hz. The broadband attenuation model provides the average lateral variation in Q_{Lg}, which extends from 10 to 600 (Figure 7a). Similar to the results for attenuation models at individual frequencies, the Arabian and Eurasian Plates still show distinct weak attenuation features, and the Anatolian, Iranian and Pamir Plateaus exhibit lower Q_{Lg}. The central Zagros orogenic belt is characterized by strong Lg attenuation, which may be related to partial melting in the lower crust caused by the Arabia-Eurasia collision and strong extrusion deformation (Zhao & Xie, 2016). The low-Q_{Lg} anomaly beneath the Zagros was also observed by Kaviani et al. (2015) and was interpreted as being influenced by the thick young sediment deposits. A higher Q_{Lg} anomaly is mainly present beneath the southeastern Zagros, which may be related to the relatively thicker crust (Figure 7b) (Manaman et al., 2011; Taghizadeh-Farahmand et al., 2015). Multiple Moho models based on receiver function (e.g., Taghizadeh-Farahmand et al., 2015), shear-wave velocity (e.g., Kaviani et al., 2020; Manaman et al., 2011), and Bouguer gravity anomaly (Jiménez-Munt et al., 2012) all observed the thicker crust beneath the Zagros orogen and Kopet-Dogh Mountains, but many details have certain differences, such as the Makran accretionary wedge and Lut Block. Some strong attenuation anomalies coincide extremely well with the Cenozoic volcanic rock outcrops (Figure 7a). Around the northern Zagros, except for the high-Q_{Lg} region near the Central Iran Basin, NW–SE-trending lower Q_{Lg} anomalies appear beneath the UDMA. In northwestern Iran, the crust beneath the Talesh Mountains, Alborz Mountains and Caspian Sea shows low-Q_{Lg} features, surrounded by the Alborz igneous outcrops and the Sahand, Sabalan and Damavand volcanoes. The eastern Alborz magmatic belt near the Kopet-Dogh Mountains also reveals a strong attenuation anomaly, and the low-Q_{Lg} anomaly extends southward to the diffuse Lut magmatic belt. The Makran magmatic arc has lower Q_{Lg}, where the Bazman, Kuh-e-Nadir and Taftan volcanoes have developed. Lg amplitudes decay strongly as seismic waves pass through the igneous crust, suggesting possible active and hot magma chambers.

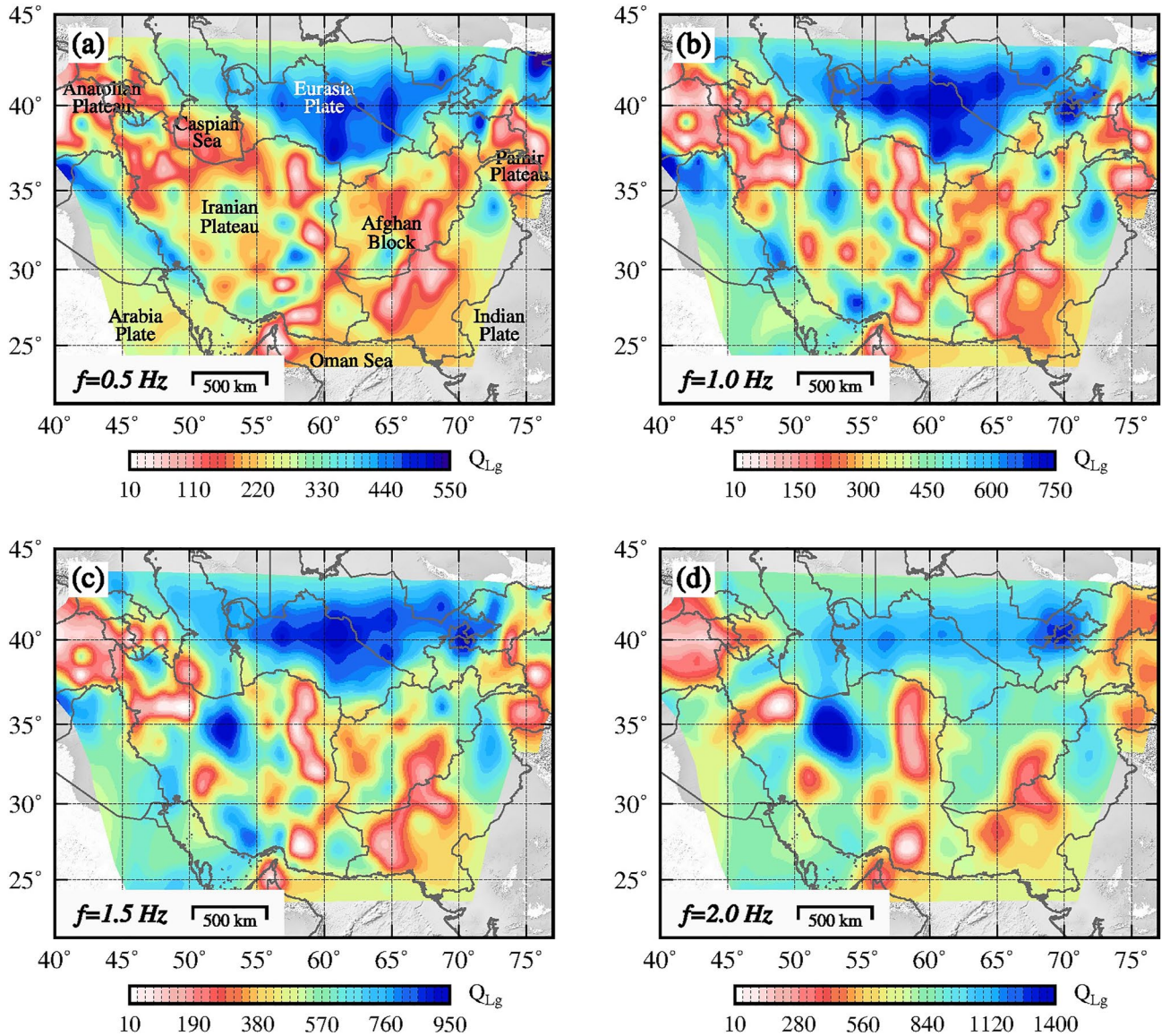

Figure 6. Selected crustal Q_{Lg} images at 0.5, 1.0, 1.5, and 2.0 Hz, where the color scales are independent for individual frequencies.

3.3. Synthetic Tests and Uncertainty Analysis

In this study, a large amount of data comes from the two linear CIGSIP arrays (Gao et al., 2022; Sadeghi-Bagherabadi et al., 2018; Wu et al., 2021). In the Lg attenuation model (Figure 6), three lower Q_{Lg} anomaly areas were observed beneath the Talesh-Alborz Mountains in the west, the Lut Block and Kopet-Dogh Mountains in the northeast, and the Makran subduction area in the southeast, where the CIGSIP stations are densely distributed (Figure 1a). To examine the effects of uneven station distribution on the tomography, two independent inversions were conducted at 1.0 Hz without and with the CIGSIP waveform data (Figures 8a and 8b). The raypath densities are also shown in Figures 8c and 8d. Without the CIGSIP stations, low-Q_{Lg} anomalies were also shown beneath the Alborz Mountains (area A), the Kopet-Dogh Mountains to Lut Block (area B), and Makran (area C); these areas are consistent with the results obtained with the CIGSIP stations (Figure 6b). However, the low Q_{Lg} beneath the CIGSIP stations is bounded more clearly and accurately delineates the crustal thermal structure beneath the volcanic rocks. With denser ray path coverage (Figure 8d), the CIGSIP station data strengthen constraints on the crustal structures in central Iran. For example, the active ZFTB was revealed as a strong attenuation zone (area D), consistent with tectonic features and previous results (e.g., Taghizadeh-Farahmand et al., 2015; Zhao

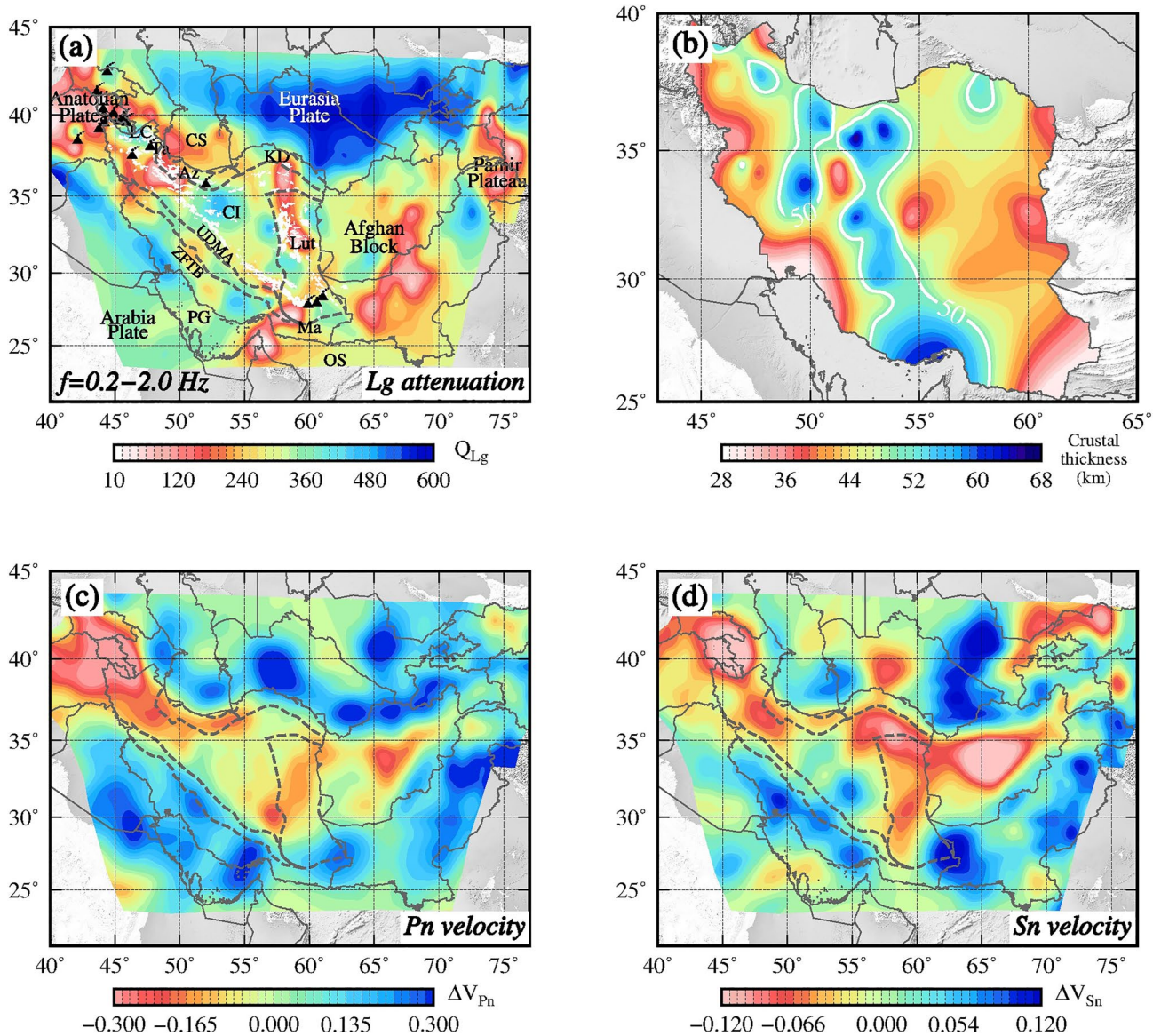

Figure 7. Broadband Lg attenuation model and comparison with other results. (a) Broadband Q_{Lg} map between 0.2 and 2.0 Hz overlain by Cenozoic volcanic rock outcrops (white areas). The black triangles denote the locations of volcanoes. (b) Crustal thickness from Taghizadeh-Farahmand et al. (2015). The white lines represent the 50-km crustal thickness contour. (c)–(d) Pn and Sn velocity tomographic results (Pei et al., 2011). The average Pn and Sn velocities are 8.04 and 4.60 km/s, respectively.

& Xie, 2016). Therefore, adding the Lg spectra from the CIGSIP stations enhances the constraints on the crustal attenuation structure of the Iranian Plateau.

To examine the authenticity and resolution of the inversion for anomalies, we developed some hypothetical anomalies with given geometries. As shown in Figure 9a, two low-Q_{Lg} regions near the Lut Block (L1) and Zagros (L2) and a high-Q_{Lg} anomaly in Central Iran (H1) were constructed. The background consists of the initial Q_{Lg} values of this region provided by two-station amplitude ratios, and the attenuation anomalies were set to ±50% perturbations. With the same stations and events, synthetic amplitudes were generated from the theoretical models, and 5% random noise was introduced (Kaviani et al., 2015). Both the shapes and magnitudes of given anomalies can be adequately retrieved (Figure 9b). Compared with L1 and L2, region H1 has sparse raypath coverage (Figure 8d) and lower resolution (Figure 4), and the amplitude of the H1 anomaly was difficult to retrieve completely. In addition, the irregular positive/negative anomalies and lateral smearing around the

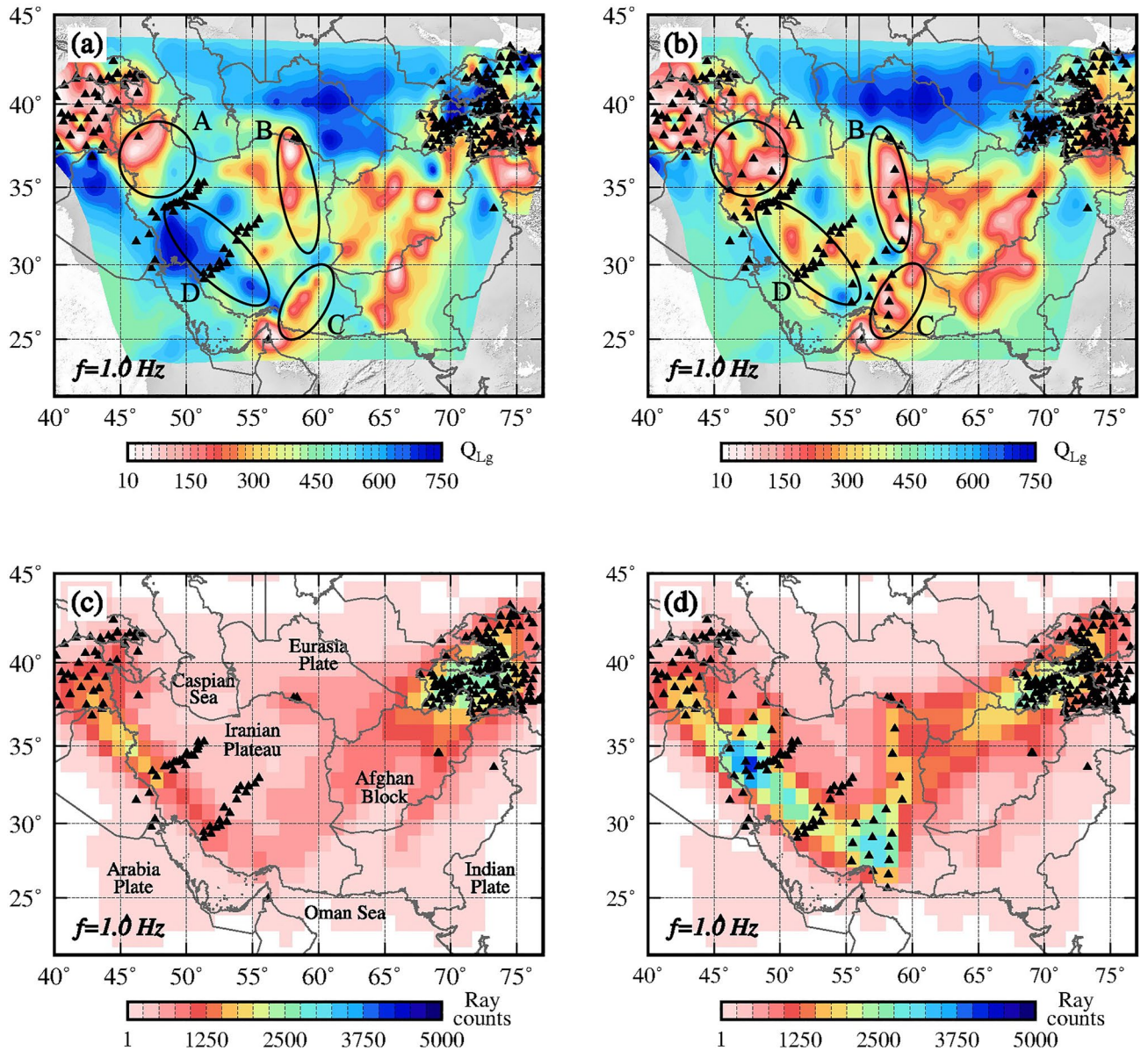

Figure 8. Maps showing the inverted Q_0 distributions obtained without using CIGSIP data (a) and with partial CIGSIP data (b) and their corresponding raypath count distributions (c) and (d), respectively. Additionally, stations (triangles) on which the recordings were used in the inversion are also labeled. Four typical areas A, B, C, and D are highlighted by circles for Q_0 comparison.

main anomalies can be caused by the irregular and sparse coverage of the seismic data and spatial aliasing of the resolution (Ronen et al., 1991). These problems could be solved if seismic data with uniform spatial distribution are available.

The uncertainties caused by the seismic data can be checked by resampling the original data set using the bootstrapping technique (Efron, 1983). We randomly selected 80% of the raypaths from the entire single- and two-station observations to construct 100 new data sets and invert the attenuation model at 58 frequencies. The mean Q_{Lg} map (Figure 10a) agrees well with the directly inverted result (Figure 7a), and the standard deviation is much smaller than the mean Q_{Lg}, ranging from 0 to 40 (Figure 10b). Therefore, the inversion system and amplitude data can provide a stable crustal attenuation structure for this region.

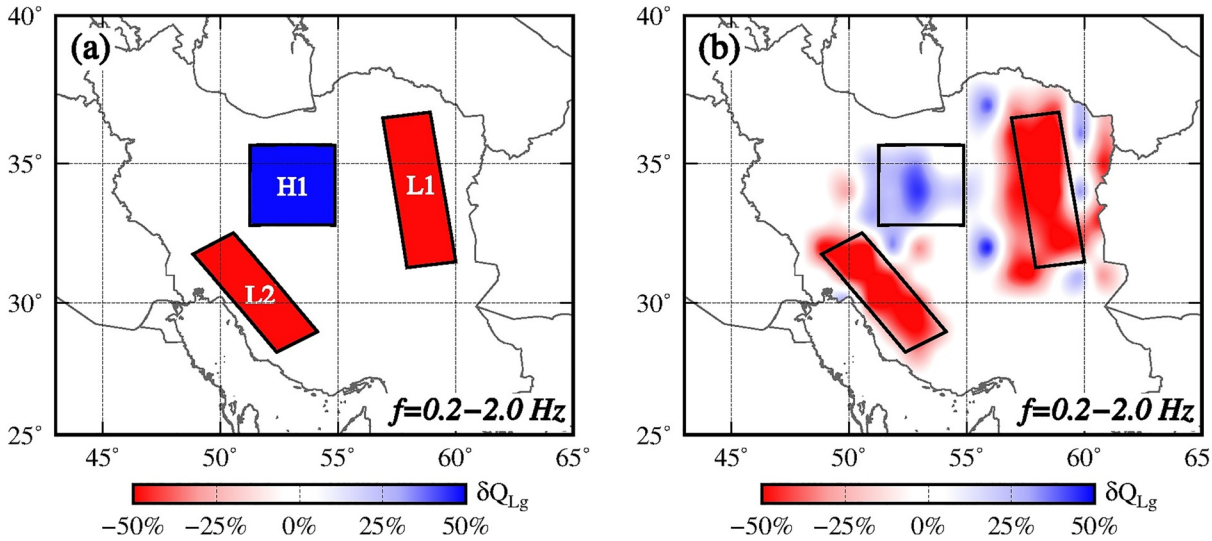

Figure 9. Reconstruction tests of the hypothetical models. (a) Synthetic model, including low-Q_{Lg} zone 1 (L1), low-Q_{Lg} zone 2 (L2) and high-Q_{Lg} zone 1 (H1). (b) Broadband inversion result for L1, L2, and H1.

4. Discussion

4.1. Comparison With Previous Studies

Several previous studies have conducted Lg attenuation tomography in and around the Iranian Plateau (Al-Damegh et al., 2004; Cong & Mitchell, 1998; Hearn, 2022; Kaviani et al., 2015; Pasyanos et al., 2009; Sandvol et al., 2001; Zhao & Xie, 2016). The Lg-coda Q_0 at 1.0 Hz ranges between 150 and 300 across the Turkish and Iranian Plateaus, and the Q_0 across the Arabian Shield and platform is approximately 300–450 (Cong & Mitchell, 1998). Similarly, previous Lg/Pg attenuation tomography also suggests that the entire Iranian Plateau appears to be a weak Lg area with Lg/Pg ratios of 1.5–2.0 (Al-Damegh et al., 2004; Sandvol et al., 2001). These results align with the low Q_{Lg} in the Iranian Plateau and the high Q_{Lg} in the Arabian Plate observed in this study. In the previous 1.0 Hz and broadband Lg attenuation models, most areas of the Iranian Plateau show lower Q_{Lg} (<300) (Kaviani et al., 2015; Pasyanos et al., 2009; Zhao & Xie, 2016). Crustal P- and S-wave attenuation imaging results also show strong attenuation throughout the whole Iranian Plateau, but more details are difficult to decipher (Pasyanos et al., 2021). Recently, Hearn (2022) conducted seismic attenuation tomography for Lg, Pg, Sn, and Pn phases

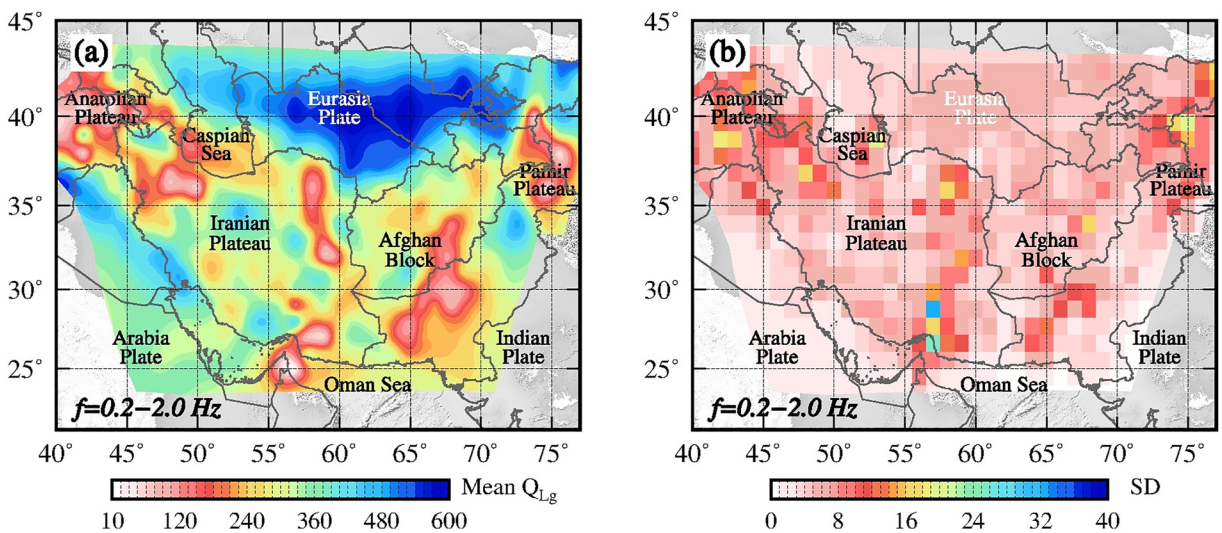

Figure 10. The mean Q_{Lg} broadband maps developed from bootstrapping (left) and the associated standard deviations (right).

in the Iranian Plateau. Both in the crust and uppermost mantle, the Iranian Plateau shows strong attenuation characteristics compared with the surrounding regions, and prominent low-Q_{Lg} anomalies are revealed beneath the UDMA, Lut Block, Kopet-Dogh Mountains and Alborz and Talesh Mountains (Hearn, 2022). The consistency of the lateral variation in Lg-wave attenuation with previous studies shows the reliability of our broadband Lg-wave attenuation model, although the Eurasian region north of the Iranian Plateau has very limited resolution. In addition, the low-Q_{Lg} region in this study constrains the active crust beneath Cenozoic volcanism well, and some high-Q_{Lg} anomalies also correspond well with stable basins and thicker crust. Our model has greater improvements due to the participation of new stations, dense raypath coverage, and accurate measurements of Lg amplitudes.

Seismic velocity tomography in the uppermost mantle was widely performed in and around the Iranian Plateau (e.g., Al-Lazki et al., 2004, 2014; Alinaghi et al., 2007; Amini et al., 2012; Hearn, 2022; Hearn & Ni, 1994; Lü et al., 2012, 2017; Mahmoodabadi et al., 2019; Pei et al., 2011). As shown in Figures 7c–7d, overall low Pn and Sn velocities were revealed in the Anatolian, Iranian, and Pamir Plateaus and Afghan Blocks (Pei et al., 2011), which corresponded well with the strong attenuation in the crust. The Eurasia region north of the Iranian Plateau showed high Pn and Sn velocities (e.g., Amini et al., 2012; Hearn, 2022; Lü et al., 2017; Pei et al., 2011). Inside the Iranian Plateau, low-velocity anomalies were mainly revealed beneath the Lut Block and Kopet-Dogh Mountains in the east and the Alborz and Talesh Mountains in the west (Pei et al., 2011), which was consistent with the Lg-wave attenuation observations. The Arabian Plate underlying the Zagros orogen and the subducting Makran subduction slab both exhibited high velocities in the uppermost mantle, which were distinguished from crustal attenuation features (e.g., Amini et al., 2012; Hearn, 2022; Lü et al., 2017; Pei et al., 2011).

4.2. Urumieh-Dokhtar Magmatic Arc

The UDMA in the Zagros orogenic belt (Figure 11a) records abundant eruptions of low-K tholeiitic and calc-alkaline magmas from the Late Cretaceous to the Paleogene (Stern et al., 2021). The Eocene–Oligocene arc volcanoes around the UDMA are generally believed to have been fed by mantle wedge melting induced by Neotethys subduction (e.g., Asadi et al., 2014). However, the formation mechanisms behind the late Cenozoic magmatism observed in the northwestern and southeastern UDMA remains controversial. Several possible models have been suggested by previous geochemical analyses of volcanic rocks, such as slab rollback (e.g., S. Babazadeh et al., 2017), changes in subduction angle (Shahabpour, 2007), slab break-off (Omrani et al., 2008), and crustal thickening (e.g., Chiu et al., 2013). Because the timing of the collision between Arabia and Eurasia is ambiguous and varies from the Late Cretaceous to the Pliocene (Mirnejad et al., 2018), it is difficult to understand the macroscopic formation mechanism of the UDMA from only age measurements and the compositional analysis of volcanic rocks. The crustal thermal structure can complement additional information for magmatic evolution (e.g., Chen et al., 2021). Strong attenuation indicates a hot and active crust beneath the UDMA, except for a relatively weak attenuation region in the central UDMA ($51-53°$E) (Figure 11b). Similar patterns of velocity anomalies were observed in this region in a previous upper crustal P-wave velocity structure (Lü & Chen, 2017) and in uppermost mantle Pn velocity tomography (e.g., Al-Lazki et al., 2004; Amini et al., 2012; Pei et al., 2011). The age distribution of igneous rocks divides the UDMA into northwestern, central, and southeastern parts, where the magmatism in the central UDMA is older than the volcanic activity in the NW and SE UDMA (Figure 12a) (Chiu et al., 2013). The strong attenuation anomalies have a certain correspondence with the variability in the age of the magmatism. Beneath the NW UDMA, the low-Q_{Lg} zone in cross-section A covers a wide frequency band of 0.2–2.0 Hz, which corresponds to the younger igneous outcrops in the UDMA and Alborz (Figure 11c). Normal Q_{Lg} is observed in the central UDMA in cross-section B (Figure 11d), whereas strong attenuation characterizes the SE UDMA within 0.2 and 1.0 Hz (Figure 11e). Lateral variations in Lg attenuation and rock age may indicate different origins of the magmatic activity.

High-velocity anomalies have been revealed up to depths of 600 km beneath central Iran by upper mantle P- and S-wave velocity tomography (Alinaghi et al., 2007; Hafkenscheid et al., 2006; Mahmoodabadi et al., 2019). The shallower high-velocity anomaly (<200 km) beneath the Zagros can be interpreted as cold Arabian mantle lithosphere, whereas the high-velocity anomaly below ~300 km is likely the remaining Neotethyan oceanic slab. The velocity cross-section through the central UDMA shows that the deeper Neotethyan oceanic slab is still connected to the shallower Arabian slab (Alinaghi et al., 2007; Hafkenscheid et al., 2006). However, significant detachment of the oceanic slabs is observed in adjacent cross-sections through the NW and SE UDMA

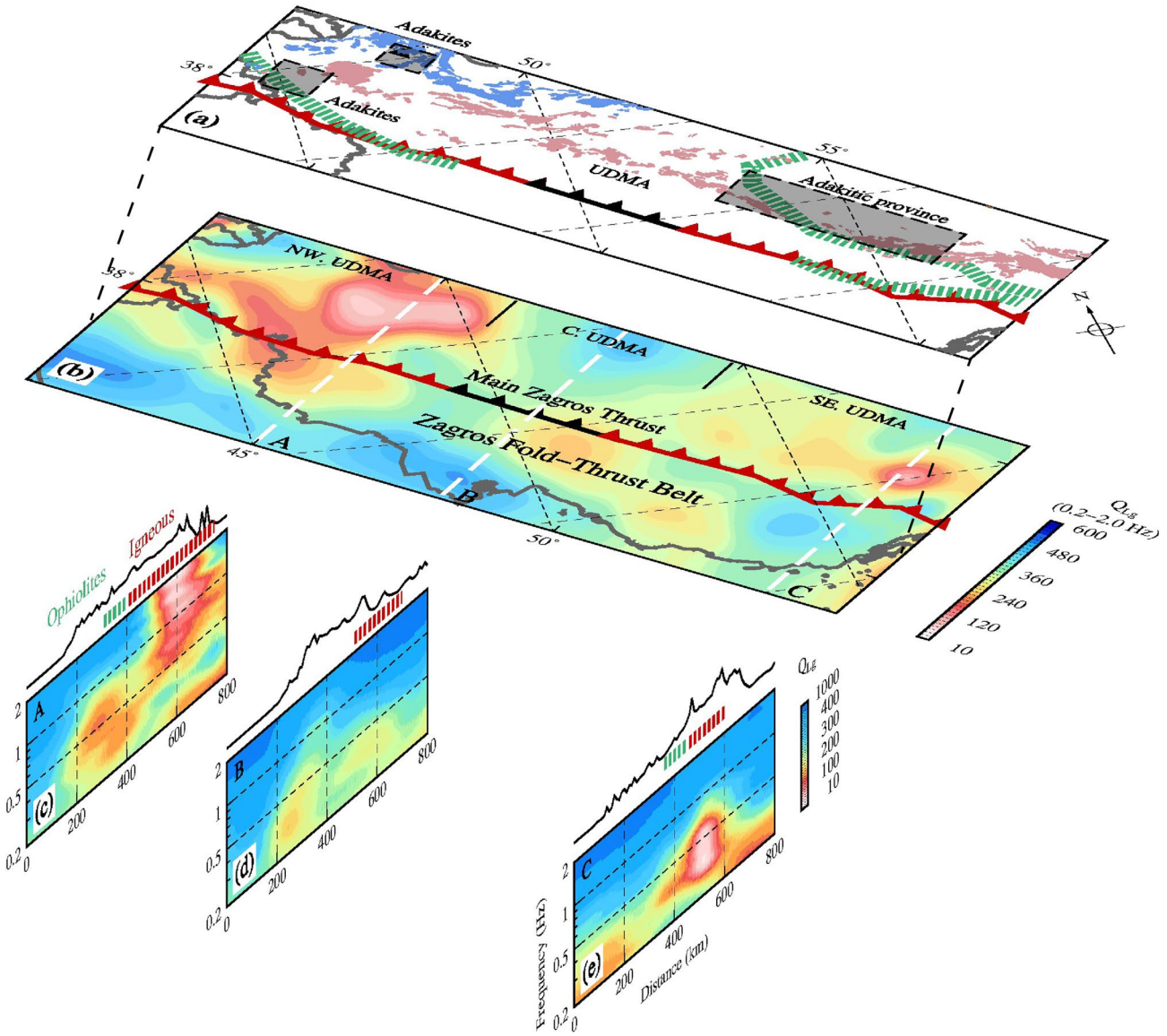

Figure 11. Broadband Q_{Lg} map and selected frequency-Q_{Lg} cross-sections around the Urumieh-Dokhtar magmatic arc (UDMA). (a) Map showing volcanic rocks near the UDMA, including Cretaceous ophiolite belts (green bands) and Cenozoic volcanic rock outcrops (same as Figure 1b). Adakitic rocks are observed in the NW and SE UDMA and are marked as shaded areas (Ghalamghash et al., 2016; Jahangiri, 2007; Omrani et al., 2008). The Main Zagros Thrust represents the suture of two continental plates, along which the Neotethys subducted beneath central Iran. The red segments represent the possible slab break-off regions (see Figure 6 in Agard et al., 2011 for details). (b) Broadband Q_{Lg} map. (c) Selected cross-sections of frequency-dependent Q_{Lg}.

(Alinaghi et al., 2007; Hafkenscheid et al., 2006; Mahmoodabadi et al., 2019). Thus, the subducted slab seems to be partially detached below Iran (red subduction lines in Figure 11), where slab detachment occurred during ~40-30 Ma under northwestern Iran but skipped central Iran and propagated southeast to Makran from 10 to 5 Ma to the present (Agard et al., 2011; Hafkenscheid et al., 2006; Omrani et al., 2008). In the NW and SE UDMA, the low-Q_{Lg} characteristics above the slab detachment regions suggest that the subducted slab relicts melt at depth due to slab break-off, which produces upwelling that intrudes into the crust. In addition, adakitic magmas are observed around the NW and SE low-Q_{Lg} regions (gray shading in Figure 11), which is related to the melting of mafic material at depth under high-temperature conditions in response to potential slab break-off (Ghalamghash et al., 2016; Jahangiri, 2007; Omrani et al., 2008). Three-dimensional numerical models have demonstrated that slab break-off is likely to occur beneath the lateral continental/oceanic transition zone (continental corner) (e.g., Li et al., 2013; Magni et al., 2017; van Hunen & Allen, 2011), and slab tear is likely first initiated away from the continental corner and then propagates along strike to the edge of the continental plate (Li et al., 2013). The NW

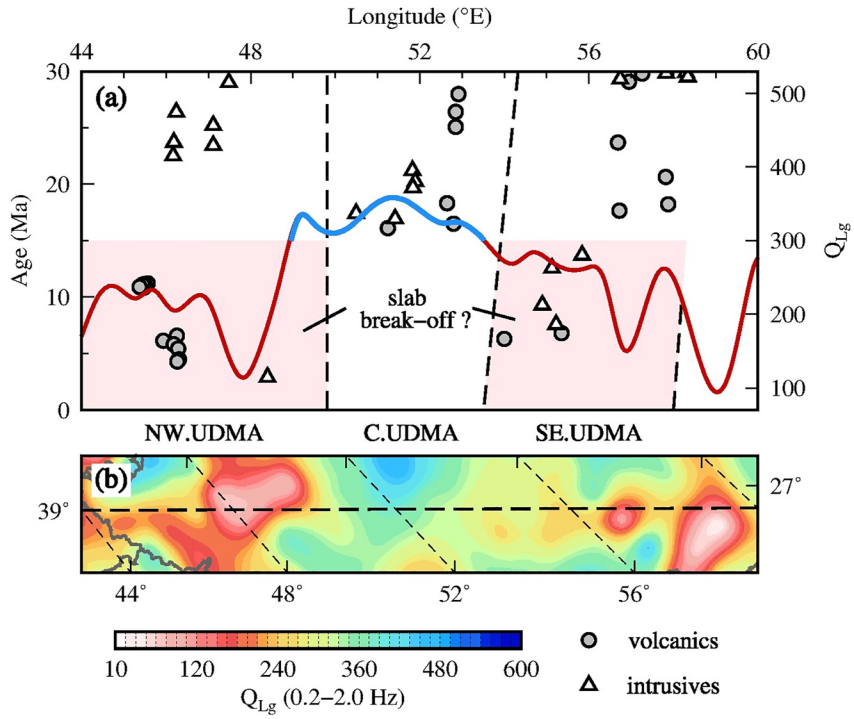

Figure 12. Age distribution of volcanic rocks in the Urumieh-Dokhtar magmatic arc (UDMA). (a) Age versus distance plot of volcanic rocks sampled from the UDMA, modified from Chiu et al. (2013). The circles and triangles represent volcanic and intrusive rocks, respectively. The solid line shows the broadband Q_{Lg} values along the thick black dashed line in b, with high Q_{Lg} (>300) shown in blue. The pink shading represents areas of possible slab break-off. (b) Broadband attenuation map along the UDMA.

and SE Zagros regions belong to typical continental corners, which are located between the eastern Mediterranean Sea subduction region and the western Makran subduction zone, respectively. This may be the reason for the lateral segmentation of slab break-off beneath the NW and SE Zagros.

Based on crucial geochemical analyses, arc magmatism ceased at ~22 Ma in the UDMA (Figure 12a), originating from typical subduction-related mantle wedge sources (Chiu et al., 2013 and references herein). The results suggested that the northwestern volcanism at ~11-3 Ma was triggered by the oblique collision after a magmatic gap of ~10 m.y., and the younger southeastern magmatism was caused by crustal thickening (Chiu et al., 2013). However, according to the age difference between the timing of the northwestern and central magmatism, it is possible that postcollisional volcanism occurred in the central UDMA after the magmatic gap but is not observed. The strong attenuation on the sides and the weak attenuation in the middle suggest that after subduction ceased, the Miocene–Quaternary magmatism was possibly activated by detachment-related mantle heat sources (Figure 12) (Alinaghi et al., 2007; Ghalamghash et al., 2016; Omrani et al., 2008). Slab detachment provides a more reasonable explanation for the abrupt reduction in the rock ages (~10 m.y.) from the central to SE UDMA. The central arc magmatism ceased at ~15 Ma and has not been reactivated.

4.3. Makran Magmatic Belt

The Makran accretionary wedge in southeastern Iran and southwestern Pakistan is an active arc system where the oceanic portion of the Arabian plate is subducted northward (hereafter Makran subduction) (Mousavi et al., 2022). The earliest stage of intraoceanic subduction of the Neotethyan Ocean led to upwelling of the asthenosphere, leaving Mesozoic lavas near Makran ophiolites (Figure 13) (Monsef et al., 2018), and Paleogene and Oligocene–Miocene volcanism migrated farther northeast (e.g., Pang et al., 2014). Neogene–Quaternary basalt ages from samples near the Bazman (~11.5-0.7 Ma), Taftan (~7.0-0.7 Ma) and Koh-i-Saltan (~5.6 Ma) arc volcanoes show a northeastward migration of volcanism (e.g., Pang et al., 2014). The Makran arc volcanism reflects the low-angle (~1–2°) or flat-slab subduction of the Arabian plate (e.g., Abedi & Bahroudi, 2016;

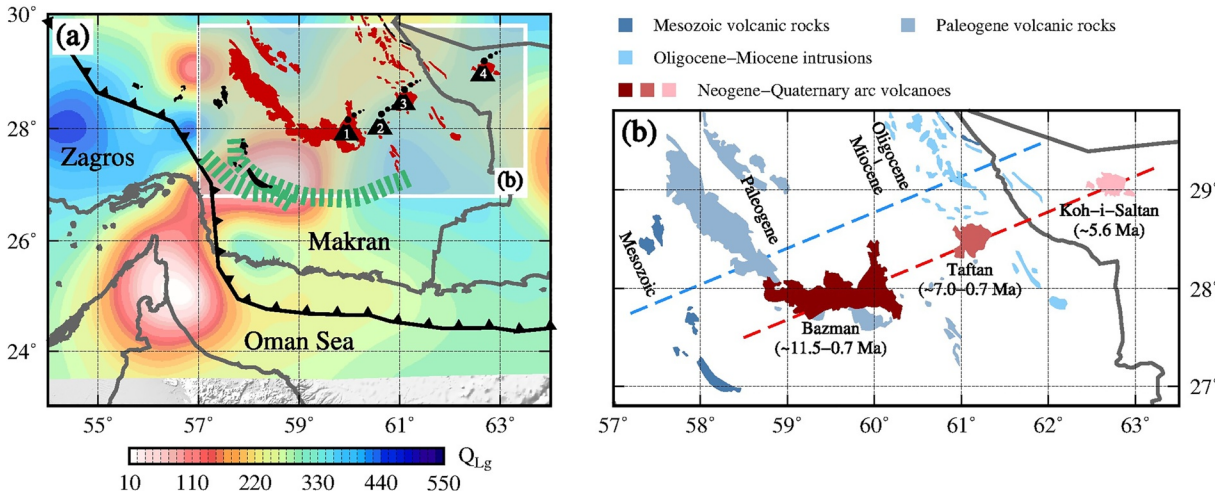

Figure 13. Distributions of Q_{Lg} and volcanic rocks in western Makran. (a) Broadband Q_{Lg} map overlain by Jurassic–Cretaceous ophiolite belts (green bands) and Cenozoic and Mesozoic volcanic rock outcrops (red and black areas). Bazman (1), Kuh-e-Nadir (2), Taftan (3) and Koh-i-Saltan (4) volcanoes are marked. (b) Volcanic rocks in western Makran (after Pang et al., 2014). The Mesozoic–Miocene volcanism (blue areas) and Neogene–Quaternary arc volcanic rocks (red areas) become younger toward the northeast.

Simmons et al., 2011). Mousavi et al. (2022) suggested that the Bazman, Taftan and Kuh-Sultan slabs represent different phases of Makran subduction prior to, simultaneous with and following slab break-off, respectively. However, the deep structure related to slab detachment has not been observed beneath the Makran region. The storage-transport processes of ascending melt under the Makran volcanic arc require more constraints from the crustal thermal structure.

Figure 13a shows a NE-trending low-Q_{Lg} anomaly belt extending from western Makran to the Lut Block in the northeast, which passes through the Jurassic–Cretaceous ophiolite belt, Mesozoic volcanic rocks, Cenozoic volcanic rocks and young stratovolcanoes. The transition zone between the Arabia–Eurasia collision and the Makran subduction zone is characterized by the strongest attenuation, which corresponds to a low Pn-velocity anomaly beneath western Makran and separated by a N–S-trending sharp boundary (at approximately 61° E) with a high-velocity zone beneath eastern Makran (e.g., Al-Lazki et al., 2014; Lü et al., 2012). According to the Lg attenuation images, we suggest that Neogene–Quaternary Makran volcanism is likely fed by subduction-related magma upwelling in the mantle wedge, which is further modified by crustal components (Pang et al., 2014). Under the Makran subduction zone, average dips of ~2° and ~3° are suggested for the western and eastern Makran oceanic crust, respectively, before it subducts under the overriding continent (Motaghi et al., 2020). Northward from this bend, dips of ~18° and ~9° are expected for western and eastern Makran, respectively (Manaman et al., 2011; Motaghi et al., 2020). Therefore, the slab at the western edge of Makran was the first to reach the depth where dehydration and melting occurred. The Paleogene–Quaternary Makran volcanism gets younger toward the NE, which is likely related to the change in subduction dip. Bazman volcano has the largest eruption scale (Figure 13b), which was supplied by, potentially, the largest magma chamber in western Makran with the strongest crustal attenuation signature. Beneath the transition zone between continental collision and oceanic subduction, the cause of strong crustal attenuation to the west of 58° E seems to be different from that of the Makran arc volcanoes. The strong attenuation beneath the transition zone could be related to slab detachment beneath the Zagros (Omrani et al., 2008), crustal deformation and rock compositional changes (Al-Lazki et al., 2014), or a potential mantle plume (Barbero et al., 2021).

4.4. Lut Magmatic Zone

The attenuation characteristics in the northeastern Iranian Plateau are well constrained by the dense broadband stations (Figure 1a). A conspicuous low-Q_{Lg} anomaly belt spans the northern Lut Block, Sabzevar zone and Kopet-Dogh Mountains (Figure 14a) and clearly delineates the Eocene–Oligocene and Pliocene–Quaternary igneous outcrops. The low-Q_{Lg} anomaly beneath the Lut region is likely associated with magmatism rather than the entire Lut Block, which is a stable solid microplate (e.g., Arjmandzadeh & Santos, 2013). Parallel to the

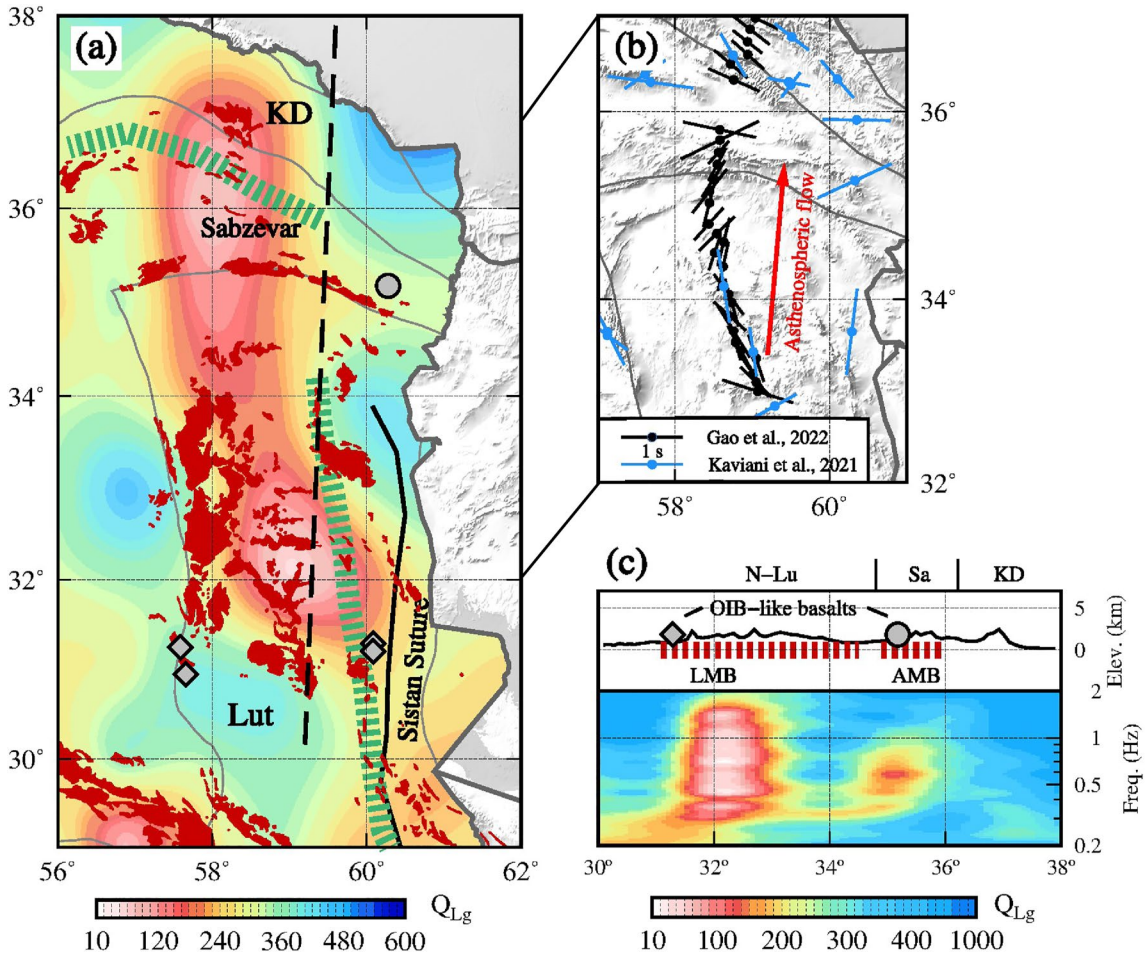

Figure 14. Broadband Q_{Lg} map of eastern Iran. (a) 0.2–2.0 Hz broadband Q_{Lg} distribution. The Cenozoic volcanic rock outcrops are shaded red. The gray circle and diamonds mark the localities of mantle xenoliths (Su et al., 2014) and modeled OIB-like alkali basalts (Walker et al., 2009), respectively. The black dashed line represents the location of the frequency-Q_{Lg} cross-section, the same as the M-M′ profile shown in previous research on S-wave receiver functions (Wu et al., 2021). (b) Lithospheric and asthenospheric anisotropy from shear-wave splitting observations of SKS, SKKS, and PKS (XKS) (Gao et al., 2022; Kaviani et al., 2021). (c) Selected frequency-Q_{Lg} cross-section. LMB, Lut magmatic belt; AMB, Alborz magmatic belt; Sa, Sabzevar zone.

Sistan suture, Cretaceous ophiolites crop out on the eastern edge of Iran and represent remnants of ancient Sistan oceanic crust. Between the Lut and Afghan Blocks, the Sistan Ocean opened in the Early Cretaceous and possibly subducted westward beneath the Lut Block during the Late Cretaceous (Moghaddam et al., 2021). The Lut volcanism is therefore suggested to have been triggered by the westward subduction of the Sistan oceanic lithosphere beneath the Lut Block, which led to the dehydration of the subducted slab (e.g., Samiee et al., 2016), the production of fluid and melt from subducted sediments (Beydokhti et al., 2015) and partial melting in the suprasubduction mantle wedge (Arjmandzadeh et al., 2011). However, $^{40}Ar/^{39}Ar$, geochemical and Sr/Nd isotope analyses suggest that the Lut magmatism was active from ~46 to ~25 Ma, which postdated the Lut–Sistan collision (Pang et al., 2013). This magmatism may have been related to the delamination of the thickened lithosphere and subsequent asthenospheric upwelling during the Eocene–Oligocene (Pang et al., 2013). The Miocene to Pliocene (~11-4 Ma) alkali basalts are further suggested to result from the partial melting of the rising asthenosphere after the delamination of the Lut lithospheric root (Pang et al., 2012).

Most Cenozoic volcanic rocks in eastern Iran crop out in the central and northern Lut Block rather than throughout the entire collision zone. The volcanic rocks and low-Q_{Lg} anomaly simultaneously deviate from the ophiolite belt and the Sistan suture zone to the north (Figure 14a). Furthermore, the eastern Iranian magmatism appears to have a diffuse pattern ~300 km wide (Pang et al., 2013), in contrast with linear or curved magmatic belts (e.g., the UDMA and Alborz ranges). Therefore, the magmatism in the Lut Block involves a special evolution mechanism.

Using the dense CIGSIP array, a strong positive velocity discontinuity is detected at ~170 km depth beneath eastern Iran by an S-wave receiver function study, possibly representing the base of an asthenospheric low-velocity layer (Wu et al., 2021). The nearby ocean island basalt (OIB) outcrops (gray circle and diamonds in Figure 14a) were presumably sourced from the asthenosphere (Su et al., 2014; Walker et al., 2009). Two relevant low-Q_{Lg} anomalies are also observed in the crust (Figure 14c), indicating that asthenospheric upwelling has changed the thermal structure in the Lut crust. NNW–SSE and NNE–SSW fast polarization directions of shear-wave splitting have been observed in eastern Iran (Figure 14b) and suggest a two-layer anisotropic structure and a northeastward asthenospheric flow beneath the Eastern Iranian Plateau, which may be induced by the contrast in lithospheric thickness with the collisional front (Gao et al., 2022). Similar seismic anisotropy of shear phases (SKS, SKKS, and PKS, called XKS) was also observed by Kaviani et al. (2021). This mantle flow pattern can explain why the hot crust with low Q_{Lg} extends to the northern Lut Block and even the Sabzevar and Kopet-Dogh regions. We suggest that the hot mantle magmas associated with Sistan subduction or the Lut–Afghan collision migrated northward driven by asthenospheric flow and accumulated beneath the northern Lut crust (Gao et al., 2022). The magma upwelling further contaminated the crust beneath the central and northern Lut Block, Sabzevar zone and even the Alborz magmatic zone and resulted in the diffuse pattern of Cenozoic magmatism. The younger Pliocene–Quaternary igneous rocks and OIB-type outcrops demonstrate that the northern Lut crust with low Q_{Lg} still has higher temperatures at present. The NW–SE fast polarization directions around the Kopet-Dogh Mountains are subparallel to the strikes of faults and orogenic belts in response to the Arabia–Eurasia collision (Gao et al., 2022), and the eastern Alborz magmatism trends in an E–W direction along the faults.

4.5. Alborz Magmatic Belt

The E–W-trending Alborz magmatism in northern Iran started in the Early Cretaceous, increased abruptly during the Eocene, and continues until the present (e.g., Asiabanha & Foden, 2012; Stern et al., 2021). The source region of Alborz magmas is generally believed to be influenced by various components, including deeply subducted lithosphere and partial melts of lithosphere in an extensional back-arc setting (Asiabanha & Foden, 2012). The crustal structures beneath the Alborz magmatic belt exhibit active and hot characteristics, where the low-Q_{Lg} anomalies span almost the entire Alborz magmatic belt, especially in the western and eastern parts. In the western Alborz, assimilation and fractional crystallization modeling indicates that the ascending magmas from a mantle source were modified by 40% crustal components (Asiabanha & Foden, 2012), which is evidenced by the low Q_{Lg} in the crust (Figure 11). The Pliocene–Quaternary Sahand, Damavand and Sabalan volcanoes are also located in the western low-Q_{Lg} region around the Talesh-Alborz Mountains (Figure 7a), suggesting multiple crustal magma chambers below. The adakitic Sabalan and Sahand volcanoes in western Alborz may be affected by mantle magma related to slab detachment. In northeastern Iran, the attenuation model cannot distinguish between the Lut magmatic zone and the eastern Alborz magmatic belt, but the centers of the two magmatic regions have the highest Q_{Lg} values (Figure 14a).

5. Conclusion and Geodynamic Implications

To detect the crustal attenuation structure in the Iranian Plateau, we performed high-resolution Lg-wave attenuation tomography using a newly compiled data set. A broadband attenuation model was constructed between 0.05 and 10.0 Hz with a resolution approaching ~1°. The Cenozoic magmatic flare-up in the Iranian Plateau is revealed by volcanic rock outcrops and effectively constrained by the strong attenuation characteristics in the crust. The low-Q_{Lg} areas are mainly observed beneath the Zagros orogenic belt, Urumieh-Dokhtar magmatic arc, Alborz rearc magmatic belt, Makran magmatic arc and Lut magmatic zone, which cover not only the active tectonic boundary belts but also the internal magmatic zone. We link the lateral variations in the crustal attenuation characteristics to Cenozoic magmatism by combining surface rock outcrops and deep seismological observations (Figure 15). In the UDMA, the arc volcanism associated with Neotethyan subduction ceased in the early Miocene (Chiu et al., 2013). The strong crustal attenuation characteristics in the northwestern and southeastern UDMA suggest that after the cessation of subduction, Miocene–Quaternary magmatism was possibly activated by slab detachment-related heat sources in the mantle (Ghalamghash et al., 2016; Jahangiri, 2007; Omrani et al., 2008). The slab detachment is supported by seismic tomographic images at greater depths (e.g., Alinaghi et al., 2007; Hafkenscheid et al., 2006; Mahmoodabadi et al., 2019). Adakitic rocks observed in the northwestern and southeastern UDMA may also be a response to potential slab break-off (Ghalamghash et al., 2016; Jahangiri, 2007;

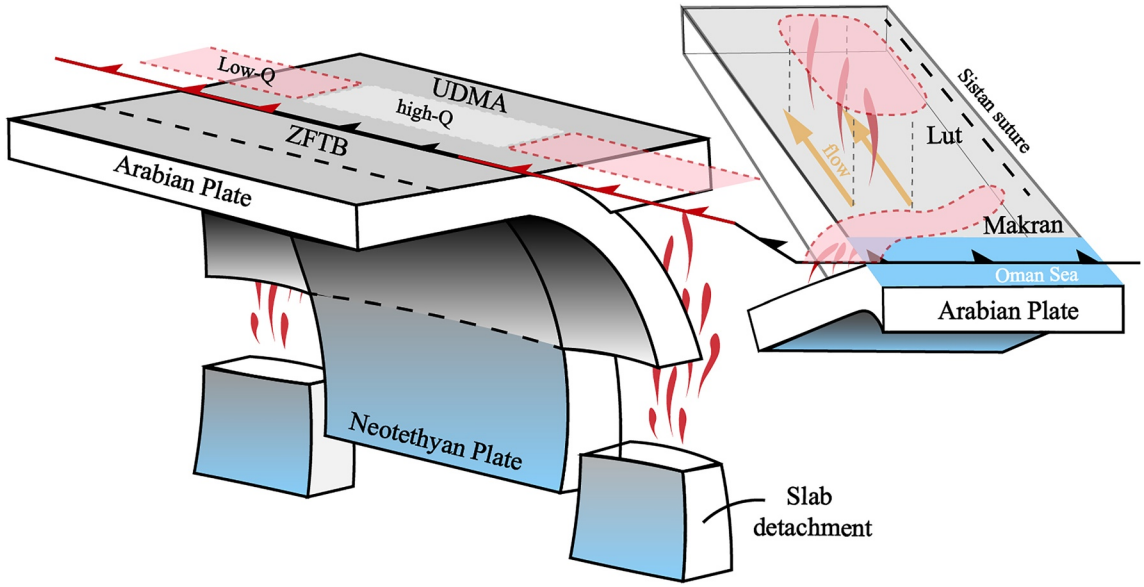

Figure 15. Schematic diagram showing the development of strong crustal attenuation structures and Cenozoic magmatism.

Omrani et al., 2008). On the southeastern edge of Iran, the NE migration of Paleogene–Quaternary Makran volcanism with SW–NE-trending crustal low-Q_{Lg} is likely related to the decrease in subduction dip from west to east. The northern Lut crust exhibits obviously strong attenuation characteristics accompanied by a large amount of diffuse Eocene–Quaternary magmatism. The hot crust and Lut magmatism may be fed by the accumulated mantle magma beneath the northern Lut driven by a possible northward asthenospheric flow, which is suggested by the asthenospheric low-velocity layer (Wu et al., 2021) and the northward polarization directions of shear-wave splitting (Gao et al., 2022; Kaviani et al., 2021). In northern Iran, the strong attenuation anomaly spans the entire E–W-trending Alborz magmatic belt, whose source likely originated from the deep mantle and crustal partial melts.

Data Availability Statement

The waveforms used in this study were collected from the Incorporated Research Institutions for Seismology Data Management Center (IRIS-DMC) and can be found at https://ds.iris.edu/wilber3/find_event (last accessed September 2022), the German Research Centre for Geoscience (GFZ) at http://geofon.gfz-potsdam.de (last accessed September 2022), the International Seismological Centre (ISC) at http://isc-mirror.iris.washington.edu (last accessed September 2022), the International Federation of Digital Seismograph Networks (FDSN) at https://www.fdsn.org (last accessed September 2022), and the China-Iran Geological and Geophysical Survey in the Iranian Plateau (CIGSIP) (Gao et al., 2022; Sadeghi-Bagherabadi et al., 2018; Wu et al., 2021). The Pn and Sn velocities used in Figure 7 were provided by Dr. S. Pei (Pei et al., 2011). The Lg waveforms from the CIGSIP stations were uploaded to the World Data Centre for Geophysics, Beijing (WDCGB) at https://doi.org/10.12197/2022GA028 (last accessed September 2022). The single- and two-station Lg amplitude data used in this study and the resulting Lg-wave attenuation model in the Iranian Plateau can be accessed on the WDCGB at https://doi.org/10.12197/2022GA015 (last accessed September 2022). Certain figures were generated using Generic Mapping Tools (GMT; https://www.generic-mapping-tools.org/).

Acknowledgments
The comments from Editor Michael Bostock, the associate editor, and two anonymous reviewers are valuable and greatly improved this manuscript. This research was supported by the National Natural Science Foundation of China (91855207, 41630210, U2139206, 41974054, and 41974061). We thank M.Y. Feng for his help in preparing the waveforms from the CIGSIP stations. The CIGSIP project was implemented following the memorandum of understanding (MOU) between IGGCAS and GSI.

References

Abedi, M., & Bahroudi, A. (2016). A geophysical potential field study to image the Makran subduction zone in SE of Iran. *Tectonophysics*, *688*, 119–134. https://doi.org/10.1016/j.tecto.2016.09.025

Agard, P., Omrani, J., Jolivet, L., Whitechurch, H., Vrielynck, B., Spakman, W., et al. (2011). Zagros orogeny: A subduction-dominated process. *Geological Magazine*, *148*(5–6), 692–725. https://doi.org/10.1017/s001675681100046x

Al-Lazki, A. I., Al-Damegh, K. S., El-Hadidy, S. Y., Ghods, A., & Tatar, M. (2014). Pn-velocity structure beneath Arabia–Eurasia Zagros collision and Makran subduction zones. *Geological Society, London, Special Publications*, *392*(1), 45–60. https://doi.org/10.1144/sp392.3

Alavi, M. (2007). Structures of the Zagros fold-thrust belt in Iran. *American Journal of Science*, *307*(9), 1064–1095. https://doi.org/10.2475/09.2007.02

Al-Damegh, K., Sandvol, E., Al-Lazki, A., & Barazangi, M. (2004). Regional seismic wave propagation (Lg and Sn) and Pn attenuation in the Arabian Plate and surrounding regions. *Geophysical Journal International*, *157*(2), 775–795. https://doi.org/10.1111/j.1365-246X.2004.02246.x

Alinaghi, A., Koulakov, I., & Thybo, H. (2007). Seismic tomographic imaging of P- and S-waves velocity perturbations in the upper mantle beneath Iran. *Geophysical Journal International*, *169*(3), 1089–1102. https://doi.org/10.1111/j.1365-246X.2007.03317.x

Al-Lazki, A. I., Sandvol, E., Seber, D., Barazangi, M., Turkelli, N., & Mohamad, R. (2004). Pn tomographic imaging of mantle lid velocity and anisotropy at the junction of the Arabian, Eurasian, and African plates. *Geophysical Journal International*, *158*(3), 1024–1040. https://doi.org/10.1111/j.1365-246X.2004.02355.x

Amini, S., Shomali, Z. H., Koyi, H., & Roberts, R. G. (2012). Tomographic upper-mantle velocity structure beneath the Iranian Plateau. *Tectonophysics*, *554–557*, 42–49. https://doi.org/10.1016/j.tecto.2012.06.009

Arjmandzadeh, R., Karimpour, M. H., Mazaheri, S. A., Santos, J. F., Medina, J. M., & Homam, S. M. (2011). Sr–Nd isotope geochemistry and petrogenesis of the Chah-Shaljami granitoids (Lut Block, Eastern Iran). *Journal of Asian Earth Sciences*, *41*(3), 283–296. https://doi.org/10.1016/j.jseaes.2011.02.014

Arjmandzadeh, R., & Santos, J. F. (2013). Sr–Nd isotope geochemistry and tectonomagmatic setting of the Dehsalm Cu–Mo porphyry mineralizing intrusives from Lut Block, eastern Iran. *International Journal of Earth Sciences*, *103*(1), 123–140. https://doi.org/10.1007/s00531-013-0959-4

Asadi, S., Moore, F., & Zarasvandi, A. (2014). Discriminating productive and barren porphyry copper deposits in the southeastern part of the central Iranian volcano-plutonic belt, Kerman region, Iran: A review. *Earth-Science Reviews*, *138*, 25–46. https://doi.org/10.1016/j.earscirev.2014.08.001

Asiabanha, A., & Foden, J. (2012). Post-collisional transition from an extensional volcano-sedimentary basin to a continental arc in the Alborz Ranges, N-Iran. *Lithos*, *148*, 98–111. https://doi.org/10.1016/j.lithos.2012.05.014

Babazadeh, S., Ghorbani, M. R., Bröcker, M., D'Antonio, M., Cottle, J., Gebbing, T., et al. (2017). Late Oligocene–Miocene mantle upwelling and interaction inferred from mantle signatures in gabbroic to granitic rocks from the Urumieh–Dokhtar arc, south Ardestan, Iran. *International Geology Review*, *59*(12), 1590–1608. https://doi.org/10.1080/00206814.2017.1286613

Babazadeh, S. A., & Wever, P. D. (2004). Early Cretaceous radiolarian assemblages from radiolarites in the Sistan Suture (eastern Iran). *Geodiversitas*, *26*, 185–206.

Barbero, E., Pandolfi, L., Delavari, M., Dolati, A., Saccani, E., Catanzariti, R., et al. (2021). The western Durkan complex (Makran accretionary prism, SE Iran): A Late Cretaceous tectonically disrupted seamounts chain and its role in controlling deformation style. *Geoscience Frontiers*, *12*(3), 101106. https://doi.org/10.1016/j.gsf.2020.12.001

Beydokhti, R. M., Karimpour, M. H., Mazaheri, S. A., Santos, J. F., & Klötzli, U. (2015). U–Pb zircon geochronology, Sr–Nd geochemistry, petrogenesis and tectonic setting of Mahoor granitoid rocks (Lut Block, Eastern Iran). *Journal of Asian Earth Sciences*, *111*, 192–205. https://doi.org/10.1016/j.jseaes.2015.07.028

Bouchon, M. (1982). The complete synthesis of seismic crustal phases at regional distances. *Journal of Geophysical Research*, *87*(B3), 1735. https://doi.org/10.1029/JB087iB03p01735

Boyd, O. S., Jones, C. H., & Sheehan, A. F. (2004). Foundering lithosphere imaged beneath the southern Sierra Nevada, California, USA. *Science*, *305*(5684), 660–662. https://doi.org/10.1126/science.1099181

Burg, J.-P. (2018). Geology of the onshore Makran accretionary wedge: Synthesis and tectonic interpretation. *Earth-Science Reviews*, *185*, 1210–1231. https://doi.org/10.1016/j.earscirev.2018.09.011

Cao, S., & Muirhead, K. J. (1993). Finite-difference modeling of Lg blockage. *Geophysical Journal International*, *115*(1), 85–96. https://doi.org/10.1111/j.1365-246X.1993.tb05590.x

Chen, Y., Gu, Y. J., Mohammed, F., Wang, J., Sacchi, M. D., Wang, R., & Nguyen, B. (2021). Crustal attenuation beneath western North America: Implications for slab subduction, terrane accretion and arc magmatism of the Cascades. *Earth and Planetary Science Letters*, *560*, 116783. https://doi.org/10.1016/j.epsl.2021.116783

Chiu, H.-Y., Chung, S.-L., Zarrinkoub, M. H., Mohammadi, S. S., Khatib, M. M., & Iizuka, Y. (2013). Zircon U–Pb age constraints from Iran on the magmatic evolution related to Neotethyan subduction and Zagros orogeny. *Lithos*, *162–163*, 70–87. https://doi.org/10.1016/j.lithos.2013.01.006

Cong, L., & Mitchell, B. (1998). Lg coda Q and its relation to the geology and tectonics of the Middle East. *Pure and Applied Geophysics*, *153*(4), 563–585. https://doi.org/10.1007/s000240050208

Efron, B. (1983). Estimating the error rate of a prediction rule: Improvement on cross-validation. *Journal of the American Statistical Association*, *78*(382), 316–331. https://doi.org/10.1080/01621459.1983.10477973

Ekstrom, G., Nettles, M., & Dziewonski, A. M. (2012). The global CMT project 2004-2010: Centroid-moment tensors for 13,017 earthquakes. *Physics of the Earth and Planetary Interiors*, *200*, 1–9. https://doi.org/10.1016/j.pepi.2012.04.002

Furumura, T., & Kennett, B. L. N. (1997). On the nature of regional seismic phases. 2. On the influence of structural barriers. *Geophysical Journal International*, *129*(2), 221–234. https://doi.org/10.1111/j.1365-246X.1997.tb01577.x

Gao, Y., Chen, L., Talebian, M., Wu, Z., Wang, X., Lan, H., et al. (2022). Nature and structural heterogeneities of the lithosphere control the continental deformation in the northeastern and eastern Iranian plateau as revealed by shear-wave splitting observations. *Earth and Planetary Science Letters*, *578*, 117284. https://doi.org/10.1016/j.epsl.2021.117284

Ghalamghash, J., Mousavi, S. Z., Hassanzadeh, J., & Schmitt, A. K. (2016). Geology, zircon geochronology, and petrogenesis of Sabalan volcano (northwestern Iran). *Journal of Volcanology and Geothermal Research*, *327*, 192–207. https://doi.org/10.1016/j.jvolgeores.2016.05.001

Hafkenscheid, E., Wortel, M. J. R., & Spakman, W. (2006). Subduction history of the Tethyan region derived from seismic tomography and tectonic reconstructions. *Journal of Geophysical Research*, *111*(B8), B08401. https://doi.org/10.1029/2005jb003791

Hatzfeld, D., & Molnar, P. (2010). Comparisons of the kinematics and deep structures of the Zagros and Himalaya and of the Iranian and Tibetan plateaus and geodynamic implications. *Reviews of Geophysics*, *48*(2), RG2005. https://doi.org/10.1029/2009rg000304

He, X., Zhao, L. F., Xie, X. B., Tian, X., & Yao, Z. X. (2021). Weak crust in southeast Tibetan Plateau revealed by Lg-wave attenuation tomography: Implications for crustal material escape. *Journal of Geophysical Research: Solid Earth*, *126*(3), e2020JB020748. https://doi.org/10.1029/2020jb020748

Hearn, T. M. (2022). Two-dimensional attenuation and velocity tomography of Iran. *Geosciences*, *12*(11), 397. https://doi.org/10.3390/geosciences12110397

Hearn, T. M., & Ni, J. F. (1994). Pn velocities beneath continental collision zones: The Turkish-Iranian Plateau. *Geophysical Journal International*, *117*(2), 273–283. https://doi.org/10.1111/j.1365-246X.1994.tb03931.x

Jahangiri, A. (2007). Post-collisional Miocene adakitic volcanism in NW Iran: Geochemical and geodynamic implications. *Journal of Asian Earth Sciences*, *30*(3–4), 433–447. https://doi.org/10.1016/j.jseaes.2006.11.008

Jiménez-Munt, I., Fernàndez, M., Saura, E., Vergés, J., & Garcia-Castellanos, D. (2012). 3-D lithospheric structure and regional/residual Bouguer anomalies in the Arabia-Eurasia collision (Iran). *Geophysical Journal International*, *190*(3), 1311–1324. https://doi.org/10.1111/j.1365-246X.2012.05580.x

Kaviani, A., Mahmoodabadi, M., Rumpker, G., Pilia, S., Tatar, M., Nilfouroushan, F., et al. (2021). Mantle-flow diversion beneath the Iranian plateau induced by Zagros' lithospheric keel. *Scientific Reports*, *11*(1), 2848. https://doi.org/10.1038/s41598-021-81541-9

Kaviani, A., Paul, A., Moradi, A., Mai, P. M., Pilia, S., Boschi, L., et al. (2020). Crustal and uppermost mantle shear wave velocity structure beneath the Middle East from surface wave tomography. *Geophysical Journal International*, *221*(2), 1349–1365. https://doi.org/10.1093/gji/ggaa075

Kaviani, A., Sandvol, E., Bao, X., Rümpker, G., & Gök, R. (2015). The structure of the crust in the Turkish–Iranian Plateau and Zagros using Lg Q and velocity. *Geophysical Journal International*, *200*(2), 1254–1268. https://doi.org/10.1093/gji/ggu468

Knopoff, L., Schwab, F., & Kauselt, E. (1973). Interpretation of Lg. *Geophysical Journal International*, *33*(4), 389–404. https://doi.org/10.1111/j.1365-246X.1973.tb02375.x

Laske, G., Masters, G., Ma, Z., & Pasyanos, M. (2013). Update on CRUST1.0—A 1-degree global model of Earth's crust. In *EGU general assembly 2013*.

Li, Z.-H., Xu, Z., Gerya, T., & Burg, J.-P. (2013). Collision of continental corner from 3-D numerical modeling. *Earth and Planetary Science Letters*, *380*, 98–111. https://doi.org/10.1016/j.epsl.2013.08.034

Lü, Y., & Chen, L. (2017). Upper crustal P-wave velocity structure beneath two volcanic areas in northern Iran. *Science China Earth Sciences*, *60*(4), 786–795. https://doi.org/10.1007/s11430-016-9005-7

Lü, Y., Liu, B., Pei, S., Sun, Y., Toksoz, M. N., & Zeng, X. (2012). Pn tomographic velocity and anisotropy beneath the Iran region. *Bulletin of the Seismological Society of America*, *102*(1), 426–435. https://doi.org/10.1785/0120100141

Lü, Y., Ni, S., Chen, L., & Chen, Q.-F. (2017). Pn tomography with Moho depth correction from eastern Europe to western China. *Journal of Geophysical Research: Solid Earth*, *122*(2), 1284–1301. https://doi.org/10.1002/2016jb013052

Magni, V., Allen, M. B., van Hunen, J., & Bouilhol, P. (2017). Continental underplating after slab break-off. *Earth and Planetary Science Letters*, *474*, 59–67. https://doi.org/10.1016/j.epsl.2017.06.017

Mahmoodabadi, M., Yaminifard, F., Tatar, M., Kaviani, A., & Motaghi, K. (2019). Upper-mantle velocity structure beneath the Zagros collision zone, Central Iran and Alborz from nonlinear teleseismic tomography. *Geophysical Journal International*, *218*(1), 414–428. https://doi.org/10.1093/gji/ggz160

Manaman, N. S., Shomali, H., & Koyi, H. (2011). New constraints on upper-mantle S-velocity structure and crustal thickness of the Iranian plateau using partitioned waveform inversion. *Geophysical Journal International*, *184*(1), 247–267. https://doi.org/10.1111/j.1365-246X.2010.04822.x

McCall, G. J. H. (1997). The geotectonic history of the Makran and adjacent areas of southern Iran. *Journal of Asian Earth Sciences*, *15*(6), 517–531. https://doi.org/10.1016/S0743-9547(97)00032-9

Mirnejad, H., Raeisi, D., McFarlane, C., Sheibi, M., & Bozkurt, E. (2018). Tafresh intrusive rocks within the Urumieh-Dokhtar magmatic arc: Appraisal of Neo-Tethys subduction. *Geological Journal*, *54*(3), 1745–1755. https://doi.org/10.1002/gj.3266

Moghaddam, M. J., Karimpour, M. H., Shafaroudi, A. M., Santos, J. F., & Corfu, F. (2021). Middle Eocene magmatism in the Khur region (Lut Block, Eastern Iran): Implications for petrogenesis and tectonic setting. *International Geology Review*, *63*(9), 1051–1066. https://doi.org/10.1080/00206814.2019.1708815

Monsef, I., Monsef, R., Mata, J., Zhang, Z., Pirouz, M., Rezaeian, M., et al. (2018). Evidence for an early-MORB to fore-arc evolution within the Zagros suture zone: Constraints from zircon U-Pb geochronology and geochemistry of the Neyriz ophiolite (South Iran). *Gondwana Research*, *62*, 287–305. https://doi.org/10.1016/j.gr.2018.03.002

Motaghi, K., Shabanian, E., & Nozad-Khalil, T. (2020). Deep structure of the western coast of the Makran subduction zone, SE Iran. *Tectonophysics*, *776*, 228314. https://doi.org/10.1016/j.tecto.2019.228314

Mousavi, N., Ardestani, V. E., & Moosavi, N. (2022). Slab extension and normal faulting in a low-angle subduction-related environment: An example of the Makran subduction zone (Iran-Pakistan). *Journal of Asian Earth Sciences*, *233*, 105244. https://doi.org/10.1016/j.jseaes.2022.105244

Omrani, J., Agard, P., Whitechurch, H., Benoit, M., Prouteau, G., & Jolivet, L. (2008). Arc-magmatism and subduction history beneath the Zagros Mountains, Iran: A new report of adakites and geodynamic consequences. *Lithos*, *106*(3–4), 380–398. https://doi.org/10.1016/j.lithos.2008.09.008

Ottemöller, L., Shapiro, N. M., Krishna Singh, S., & Pacheco, J. F. (2002). Lateral variation of Lg wave propagation in southern Mexico. *Journal of Geophysical Research*, *107*(B1), ESE3-1–ESE3-13. https://doi.org/10.1029/2001jb000206

Paige, C. C., & Saunders, M. A. (1982). LSQR: An algorithm for sparse linear equations and sparse least squares. *ACM Transactions on Mathematical Software*, *8*(1), 43–71. https://doi.org/10.1145/355984.355989

Pang, K.-N., Chung, S.-L., Zarrinkoub, M. H., Chiu, H.-Y., & Li, X.-H. (2014). On the magmatic record of the Makran arc, southeastern Iran: Insights from zircon U-Pb geochronology and bulk-rock geochemistry. *Geochemistry, Geophysics, Geosystems*, *15*(6), 2151–2169. https://doi.org/10.1002/2014gc005262

Pang, K.-N., Chung, S.-L., Zarrinkoub, M. H., Khatib, M. M., Mohammadi, S. S., Chiu, H.-Y., et al. (2013). Eocene–Oligocene post-collisional magmatism in the Lut–Sistan region, eastern Iran: Magma genesis and tectonic implications. *Lithos*, *180–181*, 234–251. https://doi.org/10.1016/j.lithos.2013.05.009

Pang, K.-N., Chung, S.-L., Zarrinkoub, M. H., Mohammadi, S. S., Yang, H.-M., Chu, C.-H., et al. (2012). Age, geochemical characteristics and petrogenesis of Late Cenozoic intraplate alkali basalts in the Lut–Sistan region, eastern Iran. *Chemical Geology*, *306–307*, 40–53. https://doi.org/10.1016/j.chemgeo.2012.02.020

Pasyanos, M. E., Matzel, E. M., Walter, W. R., & Rodgers, A. J. (2009). Broad-band Lg attenuation modelling in the Middle East. *Geophysical Journal International*, *177*(3), 1166–1176. https://doi.org/10.1111/j.1365-246X.2009.04128.x

Pasyanos, M. E., Tarabulsi, Y. M., Al-Hadidy, S. Y., Raddadi, W. W., Mousa, A. D., El-Hussain, I., et al. (2021). Improved lithospheric attenuation structure of the Arabian Peninsula through the use of national network data. *Arabian Journal of Geosciences*, *14*(10), 914. https://doi.org/10.1007/s12517-021-07294-x

Pei, S., Sun, Y., & Toksöz, M. N. (2011). Tomographic Pn and Sn velocity beneath the continental collision zone from Alps to Himalaya. *Journal of Geophysical Research*, *116*(B10), B10311. https://doi.org/10.1029/2010jb007845

Regard, V., Hatzfeld, D., Molinaro, M., Aubourg, C., Bayer, R., Bellier, O., et al. (2010). The transition between Makran subduction and the Zagros collision: Recent advances in its structure and active deformation. *Geological Society, London, Special Publications*, *330*(1), 43–64. https://doi.org/10.1144/sp330.4

Ricou, L.-E. (1994). Tethys reconstructed: Plates, continental fragments and their boundaries since 260 Ma from central America to south-eastern Asia. *Geodinamica Acta*, *7*(4), 169–218. https://doi.org/10.1080/09853111.1994.11105266

Ringdal, F., Marshall, P. D., & Alewine, R. W. (1992). Seismic yield determination of Soviet underground nuclear explosions at the Shagan River test site. *Geophysical Journal International*, *109*(1), 65–77. https://doi.org/10.1111/j.1365-246X.1992.tb00079.x

Ronen, S., Sorin, V., & Bale, R. (1991). Spatial dealiasing of 3-D seismic-reflection data. *Geophysical Journal International*, *105*(2), 503–511. https://doi.org/10.1111/j.1365-246X.1991.tb06729.x

Sadeghi-Bagherabadi, A., Sobouti, F., Ghods, A., Motaghi, K., Talebian, M., Chen, L., et al. (2018). Upper mantle anisotropy and deformation beneath the major thrust-and-fold belts of Zagros and Alborz and the Iranian Plateau. *Geophysical Journal International*, *214*(3), 1913–1918. https://doi.org/10.1093/gji/ggy233

Samiee, S., Karimpour, M. H., Ghaderi, M., Haidarian Shahri, M. R., Klöetzli, U., & Santos, J. F. (2016). Petrogenesis of subvolcanic rocks from the Khunik prospecting area, south of Birjand, Iran: Geochemical, Sr–Nd isotopic and U–Pb zircon constraints. *Journal of Asian Earth Sciences*, *115*, 170–182. https://doi.org/10.1016/j.jseaes.2015.09.023

Sandvol, E., Al-Damegh, K., Calvert, A., Seber, D., Barazangi, M., Mohamad, R., et al. (2001). Tomographic imaging of Lg and Sn propagation in the Middle East. *Pure and Applied Geophysics*, *158*(7), 1121–1163. https://doi.org/10.1007/PL00001218

Sereno, T. J., Bratt, S. R., & Bache, T. C. (1988). Simultaneous inversion of regional wave spectra for attenuation and seismic moment in Scandinavia. *Journal of Geophysical Research*, *93*(B3), 2019. https://doi.org/10.1029/JB093iB03p02019

Shahabpour, J. (2007). Island-arc affinity of the Central Iranian Volcanic Belt. *Journal of Asian Earth Sciences*, *30*(5–6), 652–665. https://doi.org/10.1016/j.jseaes.2007.02.004

Shapiro, N., Bethoux, N., Campillo, M., & Paul, A. (1996). Regional seismic phases across the Ligurian Sea: Lg blockage and oceanic propagation. *Physics of the Earth and Planetary Interiors*, *93*(3–4), 257–268. https://doi.org/10.1016/0031-9201(95)03069-7

Simmons, N. A., Myers, S. C., & Johannesson, G. (2011). Global-scale P wave tomography optimized for prediction of teleseismic and regional travel times for Middle East events: 2. Tomographic inversion. *Journal of Geophysical Research*, *116*(B4), B04305. https://doi.org/10.1029/2010jb007969

Stern, R. J., Moghadam, H. S., Pirouz, M., & Mooney, W. (2021). The geodynamic evolution of Iran. *Annual Review of Earth and Planetary Sciences*, *49*(1), 9–36. https://doi.org/10.1146/annurev-earth-071620-052109

Street, R. L., Herrmann, R. B., & Nuttli, O. W. (1975). Spectral characteristics of the Lg wave generated by central United States earthquakes. *Geophysical Journal International*, *41*(1), 51–63. https://doi.org/10.1111/j.1365-246X.1975.tb05484.x

Su, B.-X., Chung, S.-L., Zarrinkoub, M. H., Pang, K.-N., Chen, L., Ji, W.-Q., et al. (2014). Composition and structure of the lithospheric mantle beneath NE Iran: Constraints from mantle xenoliths. *Lithos*, *202–203*, 267–282. https://doi.org/10.1016/j.lithos.2014.06.002

Taghizadeh-Farahmand, F., Afsari, N., & Sodoudi, F. (2015). Crustal thickness of Iran inferred from converted waves. *Pure and Applied Geophysics*, *172*(2), 309–331. https://doi.org/10.1007/s00024-014-0901-0

van Hunen, J., & Allen, M. B. (2011). Continental collision and slab break-off: A comparison of 3-D numerical models with observations. *Earth and Planetary Science Letters*, *302*(1–2), 27–37. https://doi.org/10.1016/j.epsl.2010.11.035

Vernant, P., Nilforoushan, F., Hatzfeld, D., Abbassi, M. R., Vigny, C., Masson, F., et al. (2004). Present-day crustal deformation and plate kinematics in the Middle East constrained by GPS measurements in Iran and northern Oman. *Geophysical Journal International*, *157*(1), 381–398. https://doi.org/10.1111/j.1365-246X.2004.02222.x

Walker, R. T., Gans, P., Allen, M. B., Jackson, J., Khatib, M., Marsh, N., & Zarrinkoub, M. (2009). Late Cenozoic volcanism and rates of active faulting in eastern Iran. *Geophysical Journal International*, *177*(2), 783–805. https://doi.org/10.1111/j.1365-246X.2008.04024.x

Wu, Z., Chen, L., Talebian, M., Wang, X., Jiang, M., Ai, Y., et al. (2021). Lateral structural variation of the lithosphere-asthenosphere system in the northeastern to eastern Iranian Plateau and its tectonic implications. *Journal of Geophysical Research: Solid Earth*, *126*(1), e2020JB020256. https://doi.org/10.1029/2020jb020256

Xie, J., Gok, R., Ni, J., & Aoki, Y. (2004). Lateral variations of crustal seismic attenuation along the INDEPTH profiles in Tibet from Lg Qinversion. *Journal of Geophysical Research*, *109*(B10), B10308. https://doi.org/10.1029/2004jb002988

Xie, J. (1993). Simultaneous Inversion for source spectrum and path-Q using Lg with application to 3 Semipalatinsk explosions. *Bulletin of the Seismological Society of America*, *83*(5), 1547–1562. https://doi.org/10.1785/bssa0830051547

Yamini-Fard, F., Hatzfeld, D., Farahbod, A. M., Paul, A., & Mokhtari, M. (2007). The diffuse transition between the Zagros continental collision and the Makran oceanic subduction (Iran): Microearthquake seismicity and crustal structure. *Geophysical Journal International*, *170*(1), 182–194. https://doi.org/10.1111/j.1365-246X.2006.03232.x

Zhang, L., Zhao, L.-F., Xie, X.-B., Wu, Q.-J., & Yao, Z.-X. (2022). Lateral variations in crustal Lg attenuation in and around the Hangay Dome, Mongolia. *International Journal of Earth Sciences*, *111*(2), 591–606. https://doi.org/10.1007/s00531-021-02131-8

Zhao, L. F., & Mousavi, S. M. (2018). Lateral variation of crustal Lg attenuation in eastern North America. *Scientific Reports*, *8*(1), 7285. https://doi.org/10.1038/s41598-018-25649-5

Zhao, L.-F., & Xie, X.-B. (2016). Strong Lg-wave attenuation in the Middle East continental collision orogenic belt. *Tectonophysics*, *674*, 135–146. https://doi.org/10.1016/j.tecto.2016.02.025

Zhao, L.-F., Xie, X.-B., He, J.-K., Tian, X., & Yao, Z.-X. (2013). Crustal flow pattern beneath the Tibetan Plateau constrained by regional Lg-wave Q tomography. *Earth and Planetary Science Letters*, *383*, 113–122. https://doi.org/10.1016/j.epsl.2013.09.038

Zhao, L.-F., Xie, X.-B., Wang, W.-M., Zhang, J.-H., & Yao, Z.-X. (2010). Seismic Lg-wave Q tomography in and around northeast China. *Journal of Geophysical Research*, *115*(B8), B08307. https://doi.org/10.1029/2009jb007157

Zhao, L.-F., Xie, X.-B., Wang, W.-M., Zhang, J.-H., & Yao, Z.-X. (2013). Crustal Lg attenuation within the north China Craton and its surrounding regions. *Geophysical Journal International*, *195*(1), 513–531. https://doi.org/10.1093/gji/ggt235